Chemistry Europe
European Chemical Societies Publishing

WILEY VCH

Excellence in Chemistry Research

Announcing our new flagship journal

- Gold Open Access
- Publishing charges waived
- Preprints welcome
- Edited by active scientists

Meet the Editors of *ChemistryEurope*

Luisa De Cola
Università degli Studi di Milano Statale, Italy

Ive Hermans
University of Wisconsin-Madison, USA

Ken Tanaka
Tokyo Institute of Technology, Japan

EurJIC
European Journal of Inorganic Chemistry

Chemistry Europe
European Chemical Societies Publishing

Accepted Article

Title: Synthesis and characterization of New Mononuclear Ru (II) Polypyridine Complexes with Catalytic Activity

Authors: Analia Mercedes Peyrot, María Priscila Zelaya, Pablo Alborés, and Florencia Fagalde

To be cited as: *Eur. J. Inorg. Chem.* **2023**, e202300021

Link to VoR: https://doi.org/10.1002/ejic.202300021

WILEY VCH

10.1002/ejic.202300021

Synthesis and characterization of New Mononuclear Ru (II) Polypyridine Complexes with Catalytic Activity

Prof. Dra. Analia Mercedes Peyrot,[a] Prof. Lic. María Priscila Zelaya,[b] Prof. Dr. Pablo Alborés,[c] Prof. Dra. Florencia Fagalde[a]*

[a]INQUINOA (CONICET-UNT), Instituto de Química Inorgánica, Facultad de Bioquímica, Química y Farmacia, Universidad Nacional de Tucumán, Ayacucho 471, (T4000INI) San Miguel de Tucumán, Argentina.

[b]INFINOA (CONICET-UNT), NanoProject, Departamento de Física, Facultad de Ciencias Exactas y Tecnología, Universidad Nacional de Tucumán (UNT) and Instituto de Física del Noroeste Argentino, Av. Independencia 1800, San Miguel de Tucumán 4000, Argentina.

[c]INQUIMAE (UBA - CONICET, DQIAyQF), Universidad de Buenos Aires, Ciudad Universitaria, Pabellón 2, 3°piso, C1428EHA, Buenos Aires, Argentina.

Corresponding Author: florencia.fagalde@fbqf.unt.edu.ar

ABSTRACT

In this work we report the synthesis and physicochemical characterization of new chloro and aqua mononuclear Ru (II) complexes of formula $[Ru(LLL)(dpp)Cl]PF_6$ and $[Ru(LLL)(dpp)OH_2](PF_6)_2$ (with LLL= tpy =2,2':6',2''-terpyridine; tptz=2,4,6-tris(2-pyridyl)-1,3,5-triazine and dpp=2,3-bis(2-pyridil)pyrazine). For complex $[Ru(tptz)(dpp)Cl]PF_6$ was determined the complete structure by X-ray diffraction. Catalytic studies of aqua-complexes revealed that they are active against the water oxidation reaction at pH=1 using cerium ammonium nitrate (CAN) as sacrificial oxidant. Also, we were able to establish reaction mechanism and rate constants of each stage of the catalytic cycle, turnover frequency (TOF) and turnover number (TON). The experimental TON value for the aqua complexes was very close to theoretical value of 7.5, indicating a high degree of recovery. DFT and TD-DFT calculations of complexes were consistent with experimental results and allowed the complete assignment of its UV–Visible bands, and redox states.

INTRODUCTION

Energy and environmental problems are the most important scientific challenges of 21st century. Eighty percent of total energy consumed worldwide comes from fossil fuels,

generating greenhouse gases that affect vital environment of living beings. Therefore, it is necessary to develop new technologies capable of providing renewable, clean and continuously available energy sources. [1] The most attractive alternative today is the large-scale use of hydrogen, which is considered the "future fuel". Hydrogen production by solar water splitting, has attracted particular scientific and industrial interest due to its simple, effective and environmentally friendly characteristics.[2]–[4]

The global water splitting reaction into O_2 and H_2 (**eq. 1**) is the result of two half-reactions, the oxidation of water to oxygen (**eq. 2)** and the reduction of protons to hydrogen (**eq. 3**).[5]

$$2H_2O \rightarrow O_2 + 2H_2 \qquad \Delta G = +237.178\ \text{kJ mol}^{-1} \qquad \textbf{(1)}$$

$$2H_2O \rightarrow 4H^+ + 4e^- + O_2 \qquad E° = +1.23\ \text{vs NHE} \qquad \textbf{(2)}$$

$$4H^+ + 4e^- \rightarrow 2H_2 \qquad E° = 0\ \text{V vs NHE} \qquad \textbf{(3)}$$

The water oxidation reaction is the most challenging reaction due to its endothermicity and the intrinsic molecular complexity generated by the four consecutive oxidation and deprotonation reactions and by the synchronised rearrangement of multiple bonds to form dioxygen.[6]–[10] Therefore, in order to use the water splitting reaction in an economically competitive technology for energy generation, the development of a catalyst that reduce the activation barrier of oxidative half-reaction is required. In the last decades, several research groups have focused on the design of different type of water oxidation catalysts (WOC) which can be used in photocatalytic devices, such as transition-metal complexes, 2D layered double hydroxides (LDHs), 2D layered metal oxides, carbonitrides (MXenes), single-atom catalysts (SAC), metal-organic frameworks (MOFs), and covalent-organic frameworks (COFs).[11-19]

Both heterogeneous and homogeneous catalysts have both major advantages and disadvantages. In general, heterogeneous catalysts are more robust, can be easily prepared in high quantities and are less expensive than their homogeneous counterparts. However, they are typically slower per active site and less selective than homogeneous catalysts. On the other hand, homogeneous catalysts exhibit higher rate and selectivity and are also simpler to study. The ease of quantitative investigation of homogeneous catalysts allow elucidating their geometric/electronic structure and the mechanism of action.

In literature it is possible to find hundreds of homogeneous catalysts like transition metal complexes, with ruthenium complexes being the dominant ones.[11], [20]–[27] However,

at present, these catalysts do not satisfy the requirements of efficiency and stability. The design of more efficient and robust catalysts requires the use of different experimental techniques associated with computational calculations to understand the reaction mechanisms, identify the intermediates of the catalytic cycle and determine the different decomposition pathways.[7], [28], [37]–[40], [29]–[36]

Studies on systems based in coordination compounds suggest that water oxidation reaction takes place in four steps: **a)** catalyst activation by proton-coupled electron transfer reactions (PCET), **b)** oxygen-oxygen bond formation, promoted by the metal centre, **c)** oxygen release and **d)** catalyst regeneration. Oxygen-oxygen bond formation can occur by two mechanisms (**Scheme 1**):

- Nucleophilic attack of water to a high oxidation state metal-oxygen (M-O) group to form a hydroperoxide intermediate.
- Intra- or intermolecular coupling of two metal-oxo units (I2M) form a metal peroxo intermediate.

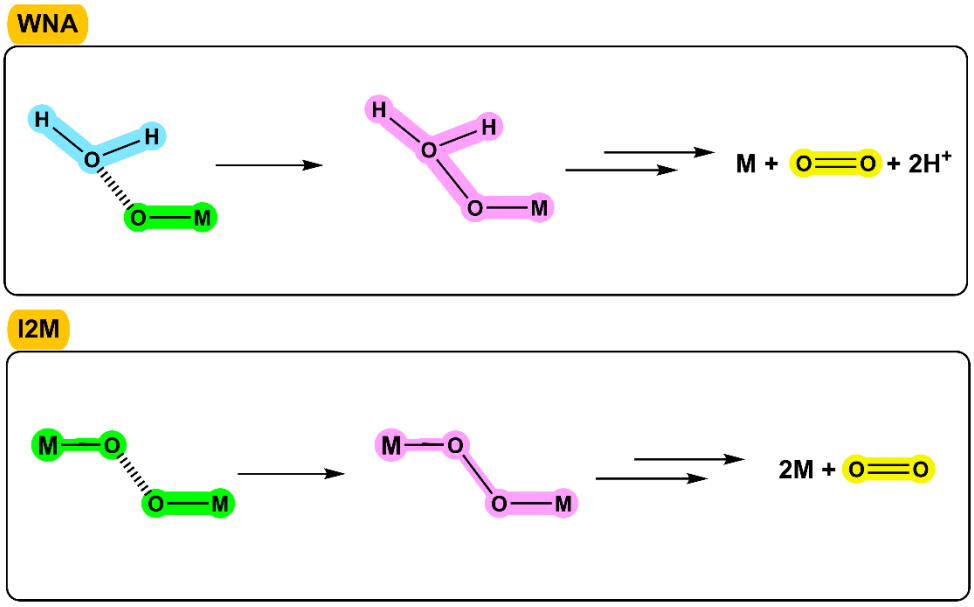

Scheme 1 – Oxygen-oxygen bond formation mechanisms promoted by transition-metal complexes.

In this work, we present the synthesis and physicochemical characterization of ruthenium (II) polypyridine complexes of molecular formula $[Ru(tpy)(dpp)Cl]PF_6.3,5H_2O$ **(1)**, $[Ru(tptz)(dpp)Cl]PF_6.\ 4H_2O$ **(2)**, $[Ru(tpy)(dpp)OH_2](PF_6)_2.3,5H_2O$ **(3)** and $[Ru(tptz)(dpp)OH_2](PF_6)_2.4H_2O$ **(4)** (with tpy=2,2':6',2''-terpyridine, tptz=2,4,6-tris(2-pyridyl)-1,3,5-triazine and dpp=2,3-bis(2-pyridyl)pyrazine). For complexes **(3)** and **(4)** kinetic and catalytic activity measurements were performed to determine mechanisms

and reaction rates of catalytic cycle and efficiency with which they can catalyse water oxidation reaction. The measurement were performed in aqueous medium at pH=1 and cerium (IV) ammonium nitrate (CAN) like sacrificial oxidant was used.

RESULTS AND DISCUSSION

SYNTHESES

The synthesis of precursors $[Ru(tpy)Cl_3]$ and $[Ru(tptz)]Cl_3$ and complexes **(1)-(4), Scheme 2,** were carried out following protocols reported in literature for similar complexes, **scheme 3**.[41]–[43]

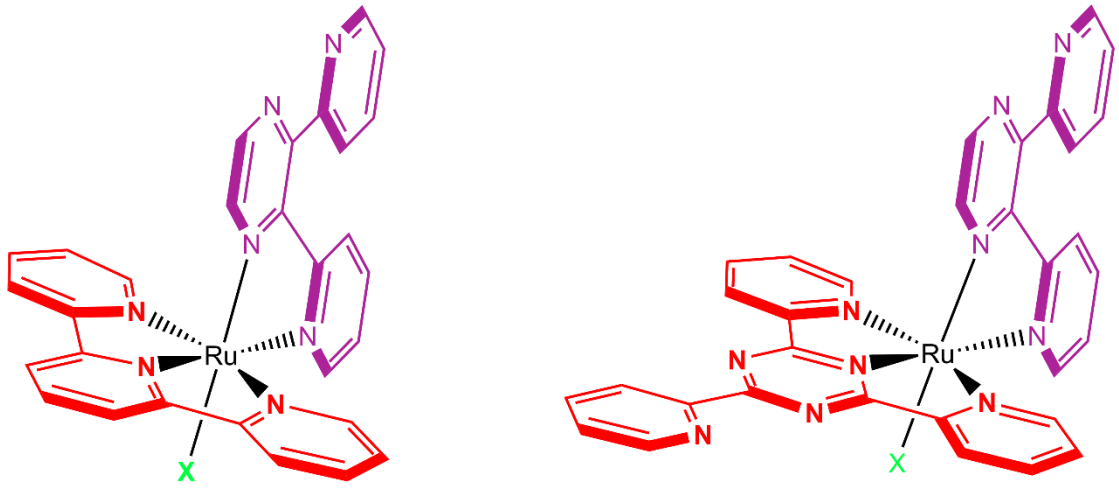

[[Ru(tpy)(dpp)X]$^{n+}$ **[Ru(tptz)(dpp)X]$^{n+}$**

X= Cl^- **n=**1 Complexes **(1)** and **(2)**
X=H_2O **n=**2 Complexes **(3)** and **(4)**

Scheme 2 - Molecular structure of complexes **(1)** to **(4)**

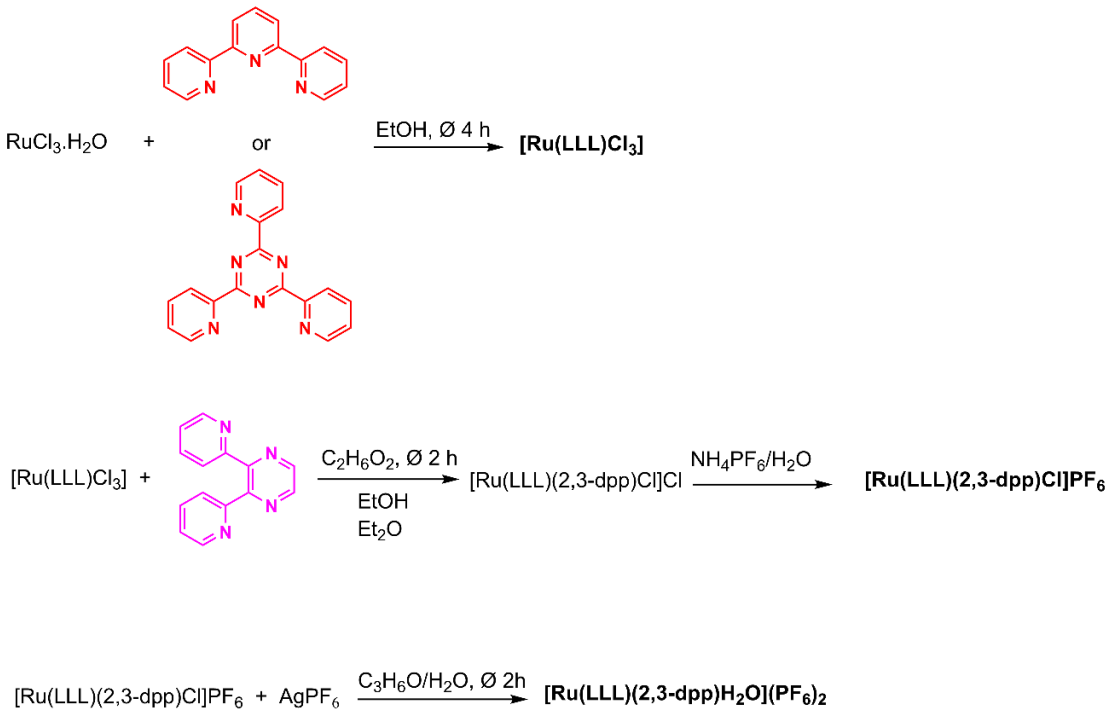

Scheme 3 – Synthesis for complexes **(1)** to **(4)**

X-RAY DIFFRACTION

Purple rod-shape crystals of complex **(2)** were obtained by slow evaporation at room temperature from a concentrated solution of complex in acetone:methanol:toluene (1:1:4 v/v). The ORTEP diagram is show in **Figure 1** and crystalline refinement data and relevant bond lengths and bond angles are summarized in **Supplementary Tables T1** and **T2**, respectively.

10.1002/ejic.202300021

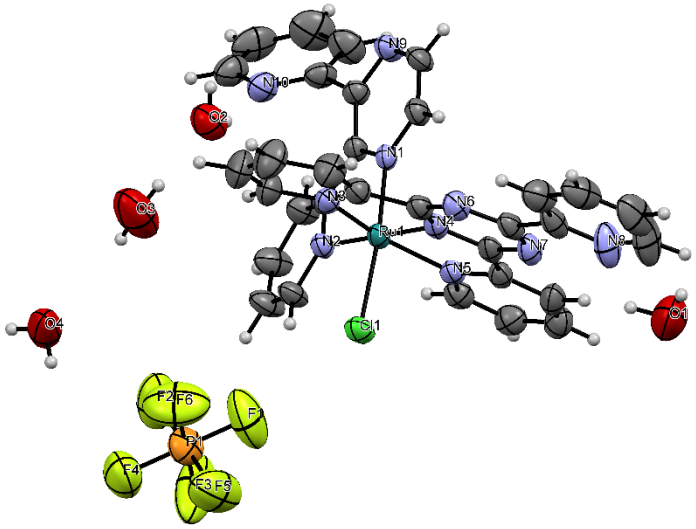

Figure 1 – ORTEP Diagram of (**2**) with thermal ellipsoids for 50% probability level, with C atoms in black, N atoms in blue and Ru atoms in green. H atoms have been omitted for clarity.

Asymmetric structure of complex **(2)** consists of a cation unit $[Ru(tptz)(dpp)Cl]^+$, a PF_6^- anion and four water molecules. The complex crystalizes in a monoclinic space group C 2/c system, where unit cell (a=23.7407 Å, b=12.4009 Å and c=25.4660 Å) contains four formula units of complex. Coordination surround corresponds to a distorted octahedral due to the presence of chelated ligands, when coordinating to ruthenium by multiple sites bonding, generates deviations from ideal angles corresponds to a regular octahedral. Tptz ligand is located in the equatorial position, with bond angles N3-Ru-N4 of 78.4 (4)° and N4-Ru-N5 of 79.3 (2)°. The dpp ligand occupied meridional position with bond angle N1-Ru-N2 of 78.0 (1)°. The sixth coordinated position is occupied for chloro. The average bond length Ru-N3 and Ru-N4 for tptz ligand is 2.0313(3) Å. The Ru-N4 bond length is relatively shorter, which could be due to donor effect of pyridine in position 4 of triazine, which generates a more effective overlap between triazine and ruthenium orbitals. For bidentate ligand, a shortening Ru-N1 bond distance with respect to Ru-N2 is observed due to the presence of uncoordinated pyridyl group at position 3 of pyrazine. The Ru-Cl bond distance is 2.392(1) Å. These data agree with those reported for similar complexes.[44]–[50]

IR SPECTROSCOPY

Supplementary Figure S1 presents FT-IR spectra of chloro-complexes **(1)** and **(2)** and aqua-complexes **(3)** and **(4)**. Between 3680-3250 cm^{-1} there is a broad band

corresponding to symmetric and asymmetric stretching of $\boldsymbol{\nu}_{O\text{-}H}$ bond. At approximately 1630 cm^{-1} a band due to deformation of $\boldsymbol{\delta}_{H\text{-}O\text{-}H}$ bond assigned to water ligand of **(3)** and **(4)** and hydration water are present in all complexes. Between 2950-1320 cm^{-1} stretching band $\boldsymbol{\nu}_{=C\text{-}H}$ and their combinations are observed. While between 1600-1320 cm^{-1} appear $\boldsymbol{\nu}_{C=C}$ and $\boldsymbol{\nu}_{C=N}$ bond stretches and between 1320-900 cm^{-1} $\boldsymbol{\delta}_{=C\text{-}H}$ in-plane deformations corresponding to polypyridine ligands. On the other hand, at 845 cm^{-1} and 560 cm^{-1} the asymmetric stretching of $\boldsymbol{\nu}_{P\text{-}F}$ bond and $\boldsymbol{\delta}_{F\text{-}P\text{-}F}$ deformation, characteristic of the PF_6^- are shown. Uniformity in positions of these bands indicates that PF_6^- anion is not coordinated to metal center, but is part of the external coordination sphere.[51]

UV-VISIBLE SPECTROSCOPY

Table 1 shows data from electronic spectra of complexes **(1) to (4)** in methanol at room temperature and their respectively assignations based on literature reported for similar complexes. [43], [44], [52]–[58] **Figure 2** presents absorption spectra of complexes **(1)** - **(4)**. All spectra consist of intense π→ π* bands centred on the ligands (IL) in ultraviolet region and metal-to-ligand charge transfer bands (MLCT) from dπ ruthenium orbitals to π* polypyridine ligands orbitals in visible region, which were confirmed by TD-DFT calculations.

The lower energy band at λ_{max}=511 nm for **(1)** and λ_{max}=492 nm for **(3)** is assigned to dπ(Ru)→π*(dpp) transition with small contributions of MLCT dπ(Ru)→π*(tpy) transition, while bands at λ_{max}=514 nm and λ_{max}=495 nm for complexes **(2)** and **(4)**, are assigned to dπ(Ru)→π*(tptz) transition with a small contribution of dπ(Ru)→π*(dpp), respectively. The introduction of a ligand with a more extended π-system leads to a bathochromic effect in MLCT bands, whereas exchange of chloro ligand for aqua generates an opposite effect.

10.1002/ejic.202300021

Table 1 – λ_{max} and ε values of absorption bands and their corresponding assignments from **(1)** to **(4)** in methanol at room temperature.

COMPLEX	MLTC $d\pi_{Ru} \rightarrow \pi^*_{ligand}$ λ[nm] (εx10⁴) [l/mol.cm]		IL $\pi \rightarrow \pi^*$ λ[nm] ε x 10⁴ [l/mol.cm]
(1)	511[a] (0.74)	473[b] (0.53)	312 (2.74), 278 sh, 273 (1.89), 235 (1.94)
(2)	514[c] (2.64)	358[a] (1.91)	289 (8.45), 245 (4.32)
(3)	492[a] (1.21)	460[b] (0.91)	307 (1.13), 270 (3.05), 240 (2.27)
(4)	495[c] (0.50)	353[a] (0.25)	286 (1.36), 244 (0.67)

[a] MLCT $d\pi_{Ru} \rightarrow \pi^*_{2,3-dpp}$, [b] MLCT $d\pi_{Ru} \rightarrow \pi^*_{tpy}$, [c] MLCT $d\pi_{Ru} \rightarrow \pi^*_{tptz}$.

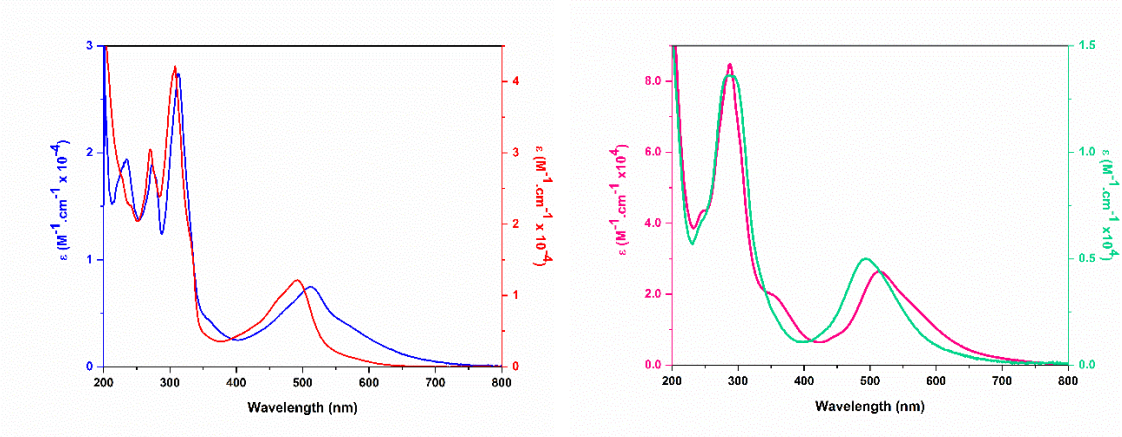

Figure 2 – a) UV-visible spectra of complexes **(1)** C=5.0x10^{-5} M and **(3)** C=5.0x10^{-5} M in methanol at room temperature. **b)** UV-visible spectra of complexes **(2)** C=3.0x10^{-5} M and **(4)** C=5.0x10^{-5} M in methanol at room temperature.

By acid-base spectrophotometric titration of complexes **(3)** and **(4)**, in Britton-Robinson buffer (mixture 0.04 M of H_3BO_3, 0.04 M of H_3PO_4 and 0.04 M of CH_3COOH) at room temperature, electronic spectra and deprotonation pK_a's of different species in equilibrium were determined. **Table 2** shows the pK_a values and **Supplementary Figures S2** and **S3** show UV-visible spectra at different pH and absorbance vs pH plots with corresponding fits for both complexes.

Table 2 – pKa's values obtaining experimentally for acid-base spectrophotometric titration in Britton-Robinson's buffer at room temperature.

COMPLEX	pK_{a1} ($dppH_2$)	pK_{a2} (dppH)	pK_{a3} (tptzH)	pK_a (H_2O)
(3)	0.66 ± 0.03	1.80 ± 0.02	----	9.65 ± 0.01
(4)	0.57 ± 0.01	1.72 ± 0.02	2.10 ± 0.03	8.62 ± 0.03

pK_{a1}: pyrazinic nitrogen from dpp, **pK_{a2}:** pyridinic nitrogen from dpp, **pK_{a3}:** pyridinic nitrogen from tptz

Complex **(3)** has three deprotonation pK_a, two corresponding to pyridinic and pyrazinic nitrogen of dpp ligand and one to deprotonation of aqua ligand. **Supplementary Figure S2a** shows that between pH= 0.06 and 0.70 the absorbance al λ_{max}=305 nm decreases while at λ_{max}=490 nm it increases. Clear isosbestic points appear indicating that first acid-base equilibrium has been reached, **eq 4**:

$$[Ru(trpy)(dppH_2)OH_2]^{4+} \overset{pK_{a1}}{\Longleftrightarrow} [Ru(trpy)(dppH)OH_2]^{3+} + H^+ \quad \textbf{(4)}$$

As pH increases to 4.26, two new bands appear at λ_{max}=230 nm and λ_{max}=239 nm. An hypsochromic shift of MLCT band occurs, due to deprotonation of pyridinic nitrogen of dpp ligand, **eq 5**:

$$[Ru(trpy)(dppH)OH_2]^{3+} \overset{pK_{a2}}{\Longleftrightarrow} [Ru(trpy)(dpp)OH_2]^{2+} + H^+ \quad \textbf{(5)}$$

From the plot of absorbance $\lambda_{489}/\lambda_{529}$ versus pH in a range from 0.06 to 4 and by fitting with three-species model, pK_{a1} and pK_{a2} values were obtained, **Supplementary Figure S2 c**.

At pH>9.00 the third acid-base equilibrium is reached due to deprotonation of aqua ligand, which is evidenced by a red shift of MLCT and IL bands (**Supplementary Figure S2 b**), as a consequence of higher donor capacity of hydroxo ligand with respect to aqua ligand, **eq 6**.

$$[Ru(trpy)(dpp)OH_2]^{2+} \overset{pK_a}{\Longleftrightarrow} [Ru(trpy)(dpp)OH]^{+} + H^+ \quad \textbf{(6)}$$

From the plot of absorbance $\lambda_{489}/\lambda_{529}$ versus pH in a range from 6 to 14 and by fitting with two-species model, a value of pK_a =9.65 ± 0.01 was obtained (**Supplementary Figure**

S2 d).This value is similar to that obtained by Meyer et al. for $[Ru(tpy)(bpm)OH_2]^{2+}$ [59] and lower than that obtained for $[Ru(tpy)(bpy)OH_2]^{2+}$ [60] in agreement with higher π-acceptor character of dpp which makes $[Ru(tpy)(dpp)OH_2]^{2+}$ more acidic.

For complex **(4)**, similar equilibria are observed in combination with deprotonation of pyridinic nitrogen of tptz ligand. The presence of tptz ligand affects the acidity of aqua, $dppH_2$ and dppH ligands due to the higher π-acceptor capacity of tptz with respect to tpy, which is evidenced by a decrease in deprotonation pK_a values. As can be seen in **Supplementary Figure S3 a**, between pH 0 to 0.06, both IL and MLCT bands absorbance decreases and a slight blue shift occurs, while a clear isosbestic point at λ_{max}=508 nm appears, indicating that the first acid-base equilibrium has been reached, **eq 7**.

$$[Ru(tptzH)(dppH_2)OH_2]^{5+} \overset{pK_{a1}}{\Longleftrightarrow} [Ru(tptzH)(dppH)OH_2]^{4+} + H^+ \quad \textbf{(7)}$$

At 0.6 < pH < 2 pyridinic nitrogen deprotonation of dpp ligand occurs, **eq. 8**.

$$[Ru(tptzH)(dppH)OH_2]^{4+} \overset{pK_{a2}}{\Longleftrightarrow} [Ru(tptzH)(dpp)OH_2]^{3+} + H^+ \quad \textbf{(8)}$$

From the plot of absorbance at λ_{max}=494 nm versus pH in a range from 0 to 2.0 and by fitting with three-species model pK_{a1} and pK_{a2} values were obtained (**Supplementary Figure S3 c**).

At pH > 2, MLCT band becomes more defined and blue-shifted due to deprotonation of tptz ligand, in agreement with lower π-acceptor character of tptz with respect to tptzH, **eq. 9**.

$$[Ru(tptzH)(dpp)OH_2]^{3+} \overset{pK_{a3}}{\Longleftrightarrow} [Ru(tptz)(dpp)OH_2]^{2+} + H^+ \quad \textbf{(9)}$$

Aqua ligand deprotonation occurs at pH>8,50 (**Supplementary Figure S3 b**). A new band appear at λ_{max}=376 nm and a red-shift of MLCT band is observed. Between λ_{max}=330 nm and λ_{max}=550 nm three isosbestic point are observed, indicating that a new equilibrium is reached, **eq 10**. Fron the plot of absorbance at λ_{max}=532 nm versus pH in a range from 2.0 to 12.0 and by fitting with three-species model pK_{a3} and pK_a values were obtained (**Supplementary Figure S3 d**).

$$[Ru(tptz)(dpp)OH_2]^{2+} \overset{pK_a}{\Longleftrightarrow} [Ru(tptz)(dpp)OH]^{+} + H^{+} \quad \textbf{(10)}$$

pK_a values found are similar to those reported by Dominguez et al. for similar complexes.[58]

ELECTROCHEMISTRY

Figure 3 shows cyclic voltammogram (CV) and differential pulse voltammogram (DPV) of complexes **(1)** and **(2)**. Both complexes show a quasi-reversible wave assigned to the couple Ru^{III}/Ru^{II} with half-wave potential $E_{1/2}$=1.03 V and 1.16 V (vs Ag/AgCl in CH_3CN, 0.1 M TBAH, v=100 mVs^{-1}) respectively, and three reduction waves centred on polypyridine ligands.

For complex **(1)**, first and second reduction waves were assigned to dpp^0/dpp^- and dpp^-/dpp^{2-} redox couple, while third reduction processes correspond to tpy^0/tpy^-. For complex **(2)**, first and third reduction waves are localized in tptz ligand and second on dpp ligand, which becomes difficult to reduce due to strong π back-donation to tptz. On the other hand, **(2)** is more difficult to oxidise than **(1)** by approximately 130 mV, as a consequence of higher π acceptor character of tptz ligand with respect to tpy ligand, which tends to stabilise HOMO orbital as we discuss in **section 2.9**

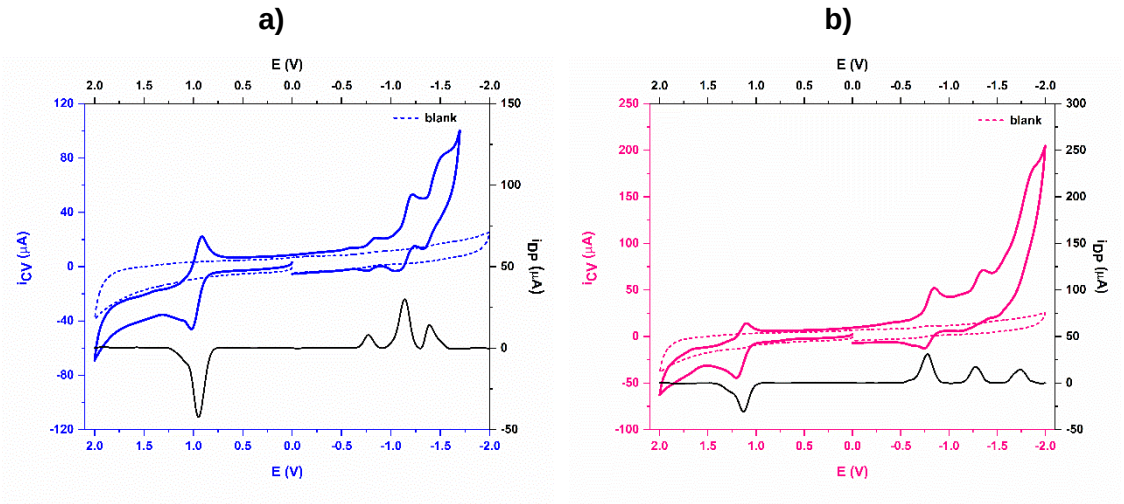

Figure 3 – Cyclic Voltammogram (CV) (coloured line) and differential pulse voltammogram (DPV) (black line) in CH_3CN 0.1 M TBAH, v=100mV/s. **a)** Complex **(1)** C=2.0x10^{-3} M. **b)** Complex **(2)** C=2.0x10^{-3} M.(In both cases dot line is the supporting electrolyte in CH_3CN 0.1M TBAH)

While, for complexes **(3)** and **(4)** the oxidation wave is shifted towards more positive potentials values due to presence of aqua ligands in sixth coordination position which stabilized t_{2g}* orbitals, **Supplementary Figure S4**.

Table 3 shows the potential values found with corresponding assignations for complexes **(1)** to **(4)** in organic environment. The assignments were done comparing with potentials reported for $Ru(LLL)_2]^{2+}$, $[Ru(LL)_3]^{2+}$ [61]–[64] and for similar complexes[44] and respect to the free ligands.[62], [65]

Table 3 – Redox Potentials for complexes **(1)** to **(4)** obtained from CV. WE: C vitreous, CE: platinum wire, RE: Ag/AgCl (3 M NaCl).

COMPLEX	$E_{1/2}$ (ΔE)‡ [V]	ASSIGNMENTS
(1)	+1.03 (0.24)[a] -0.88 (0.07)[a] -1.11 (0.20)[a] -1.40 (0.24)[a]	Ru^{III}/Ru^{II} dpp^0/dpp^- dpp^-/dpp^{2-} tpy^0/tpy^-
(2)	+1.16 (0.13)[a] -0.81 (0.10)[a] -1.24 (0.21)[a] -1.54 (0,11)[a]	Ru^{III}/Ru^{II} $tptz^0/tptz^-$ dpp^0/dpp^- $tptz^-/tptz^{2-}$
(3)	+1.18 (0.08)[b]	Ru^{III}/Ru^{II}
(4)	+1.32 (0.19)[b]	Ru^{III}/Ru^{II}

‡$\mathbf{\Delta E = E_{pd} - E_{pi}}$

[a] CH_3CN 0.1 M TBAH, [b] CH_2Cl_2 0.1 M TBAH.

From electrochemical measurements of aqua-complexes **(3)** and **(4)** carried out in Britton-Robinson buffer, corresponding Pourbaix diagrams were done. These diagrams bring information about regions where different redox and acid-base species exist, which were assigned by linear regression analysis using Nernst equation for PCET processes ($E = E° + 0.059\ \frac{m}{n}\ pH$ with m: protons transferred number and n: electrons transferred number) [66] and data reported in literature for similar Ru (II) complexes. [27], [43], [58], [59], [67], [68]

For the aqua-complex **(3)**, **Figures 4** show the Pourbaix diagram while **Figure 5** the cyclic and differential pulse voltammograms at pH=1.48, 5.25 and 10.10.

At 1 < pH <$pK_{a2(dppH)}$ complex suffer a quasi-reversible oxidation process (ΔE=110 mV), **Figure 5 a**, assigned to redox pair $[Ru^{IV} = O]^{2+}/[Ru^{II} - OH_2]^{3+}$ while deprotonation of dppH ligand bound to Ru(IV) occurs at pH<1, **eq 11** and 1**2**.

$$[(tpy)(dppH)Ru^{IV} = O]^{3+} + 2H^+ + 2e^- \rightarrow [(tpy)(dppH)Ru^{II}OH_2]^{3+} \quad \textbf{(11)}$$

$$[(\mathrm{tpy})(\mathrm{dpp})\mathrm{Ru}^{\mathrm{IV}}=\mathrm{O}]^{2+} + \mathrm{H}^{+} \rightarrow [(\mathrm{tpy})(\mathrm{dppH})\mathrm{Ru}^{\mathrm{IV}}=\mathrm{O}]^{3+} \quad \textbf{(12)}$$

At 1.8<pH<$pK_{a(OH2)}$ cyclic voltammogram show a reversible oxidation wave (ΔE=92 mV) assigned to redox couple $[\mathrm{Ru}^{\mathrm{IV}}=\mathrm{O}]^{2+}/[\mathrm{Ru}^{\mathrm{II}}-\mathrm{OH}_2]^{2+}$, **eq 13**.

$$[\mathrm{Ru}^{\mathrm{IV}}(\mathrm{tpy})(\mathrm{dpp})=\mathrm{O}]^{2+} + 2\mathrm{H}^{+} + 2\mathrm{e}^{-} \rightarrow [\mathrm{Ru}^{\mathrm{II}}(\mathrm{tpy})(\mathrm{dpp})\mathrm{OH}_2]^{2+} \quad \textbf{(13)}$$

Both processes are pH-dependent with slope value equal to 50 mV/pH corresponding to an oxidation process, which involves $2H^+/2e^-$ PCET in agreement with expected theoretical value of 59 mV/pH according to Nernst equation.

Finally, at pH > $pK_{a(OH2)}$ a reversible oxidation wave (ΔE=80 mV) corresponding to redox couple $[\mathrm{Ru}^{\mathrm{IV}}=\mathrm{O}]^{2+}/[\mathrm{Ru}^{\mathrm{II}}-\mathrm{OH}]^{+}$ is observed. This process is pH-dependent with slope value of 25 mV/pH which indicates $1H^+/2e^-$ PCET, **eq 14**.

$$[(\mathrm{tpy})(\mathrm{dpp})\mathrm{Ru}^{\mathrm{IV}}=\mathrm{O}]^{2+} + \mathrm{H}^{+} + 2\mathrm{e}^{-} \rightarrow [(\mathrm{tpy})(\mathrm{dpp})\mathrm{Ru}^{\mathrm{II}}(\mathrm{OH})]^{+} \quad \textbf{(14)}$$

At E=1.25 V a strong decay in current intensity is observed, which coincides with second oxidation wave present in differential pulse voltammograms. This pH-independent process is assigned to redox pair $[\mathrm{Ru}^{\mathrm{V}}=\mathrm{O}]^{3+}/[\mathrm{Ru}^{\mathrm{IV}}=\mathrm{O}]^{2+}$ and it attributed to onset of catalytic water oxidation, **equation 15**.

$$[(\mathrm{tpy})(\mathrm{dpp})\mathrm{Ru}^{\mathrm{V}}=\mathrm{O}]^{3+} + \mathrm{e}^{-} \rightarrow [(\mathrm{tpy})(\mathrm{dpp})\mathrm{Ru}^{\mathrm{IV}}=\mathrm{O}]^{2+} \quad \textbf{(15)}$$

10.1002/ejic.202300021

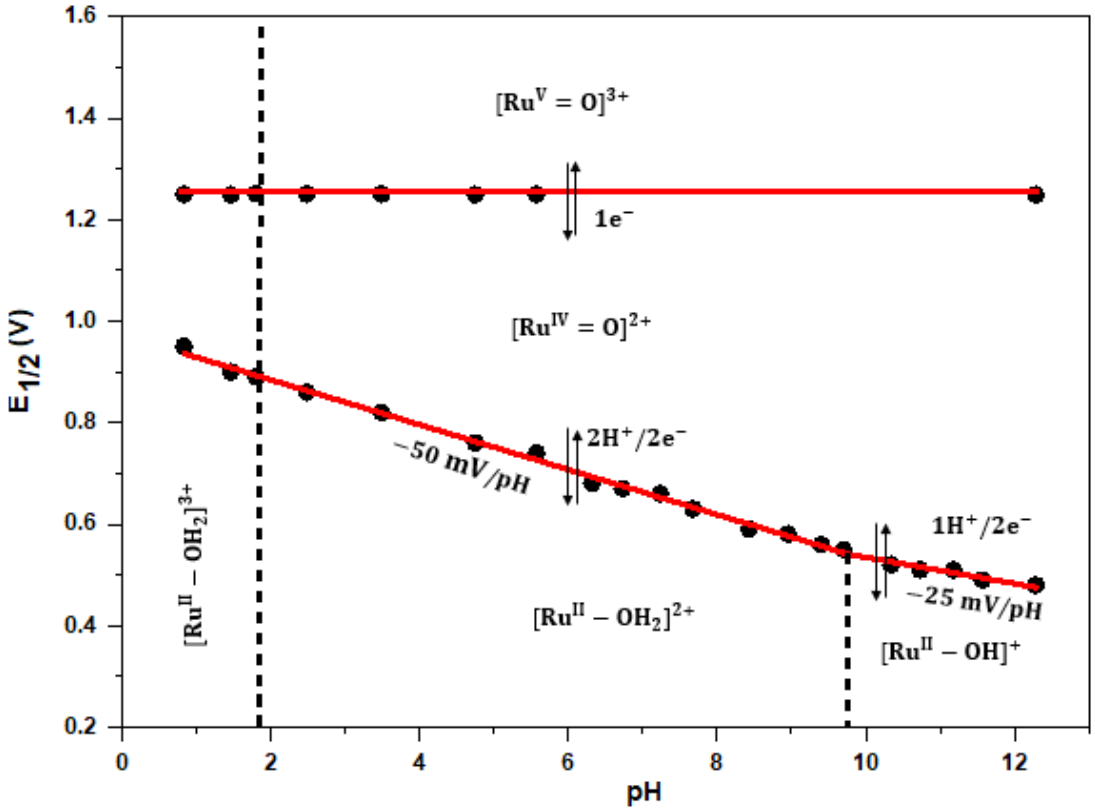

Figure 4 – Pourbaix diagram of complex **(3)** C=1.0x10^{-3} M in Britton-Robinson buffer. The black dots correspond to potentials values extracts from cyclic voltammogram and red lines correspond to lineal regression fit. Dash lines indicate pK_a values obtained by spectrophotometric acid-base titration.

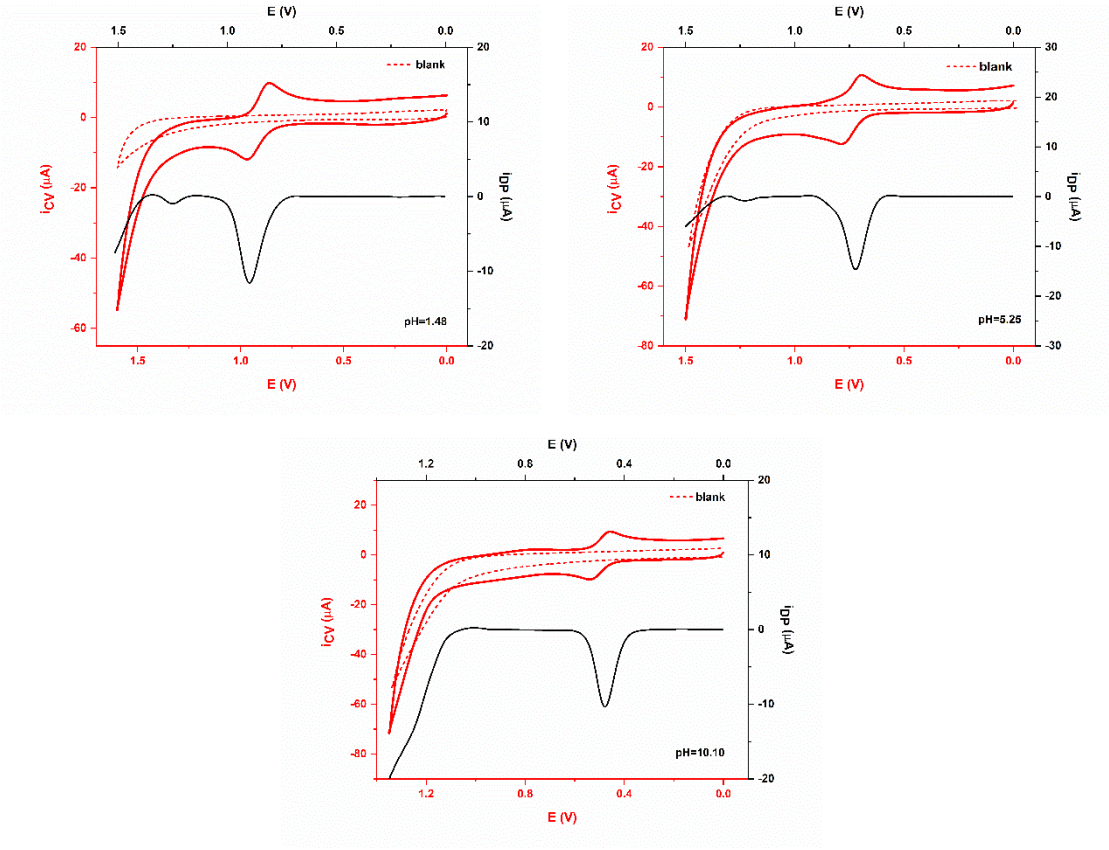

Figure 5 – Cyclic voltammogram (red line) and differential pulse voltammogram (black line) of complex **(3)** C=1.0x10^{-3} M, v=100 mV/s, in Britton-Robinson buffer at different pHs. Dot line correspond to the supporting electrolyte.

Complex **(4)** presents similar behaviour to **(3)**. **Supplementary Figure S5** presents the corresponding Pourbaix diagram and **Supplementary Figure S6** shows cyclic voltammograms and differential pulse voltammograms at pH=1.31, 6.76 and 10.50.

Controlled-potential electrolysis measurements at pH=1.0 in 0.1 M $HClO_4$ at E=0.95 V and 1.30 V for complex **(3)** gave a value of two and three electrons transferred, respectively. Same results were obtained for complex **(4)** when E=1.05 V and 1.30 V were applied, **Supplementary Figure S7**.

Both aqua-complexes present a “missing" oxidation state. $[Ru^{III}\text{-}OH]^{2+}$ intermediate is unstable with respect to the disproportionation into $[Ru^{IV}\text{=}O]^{2+}$ and $[Ru^{II}\text{-}OH_2]^{2+}$ because the potentials for the Ru^{IV}/Ru^{III} and Ru^{III}/Ru^{II} redox couples are very close, resulting in a single pH-dependent oxidation wave as a consequence of the $2H^+/2e^-$ PCET,[59], [69], [70] in agreement with charge value obtained by EPC. In contrast, in $[Ru(tpy)(bpy)OH_2]^{2+}$ [43] and $[Ru(Me_2Ntpy)(bpy\text{-}OMe)(OH_2)]^{2+}$[25] (with bpy= 2,2’-bipyridine y Me2Ntpy= 4’-N,N-dimethylamino-2,2’:6’,2”-terpyridine y bpy-OMe= 4,4’-dimethoxy-2,2’-bipyridine)., $[Ru^{III}\text{-}OH]^{2+}$ specie appear as a stable intermediate because $\Delta E_{Ru^{III}/Ru^{II}}$ is 190 mV and 430 mV, respectively.

UV-VISIBLE SPECTROELECTROCHEMISTRY AND SPECTROPHOTOMETRIC REDOX TITRATION

Pourbaix diagrams assignments at pH=1 of complexes **(3)** and **(4)**, were confirmed by UV-visible spectroelectrochemistry measurements and spectrophotometric redox titration in $HClO_4$ 0.1 M.

Figure 6 presents absorption spectra of complex **(3)** at pH=1, after control potential electrolysis (CPE) at E=0.91 and 1.30V.

At E=0.91 V, IL (λ_{max} = 271 nm and 309 nm) and MLCT (λ_{max}=500 nm) bands absorbances decrease and redshift due to metal centre oxidation. Between λ_{max}=350 and 600 nm an isosbestic point is evident suggesting the presence of two species in equilibrium. This oxidation process results in a charge value of Q= $2.18.10^{-3}$ C/mol consistent with 2 electron transfer, which is assigned to redox couple $[Ru^{IV}=O]^{2+}$/ $[Ru^{II}\text{-}OH_2]^{3+}$.

At E=1.30 V, complete bleaching of MLCT band occurs as a consequence of oxidation of the metal centre from Ru^{IV} to Ru^{V}. On the other hand, the absorbance of IL band at λ_{max}=309 nm falls below the absorbance at λ_{max}=270 nm. When a potential of E=0 V is applied to the solution, initial spectrum is recovered by 80 % indicating that the oxidation process is reversible.

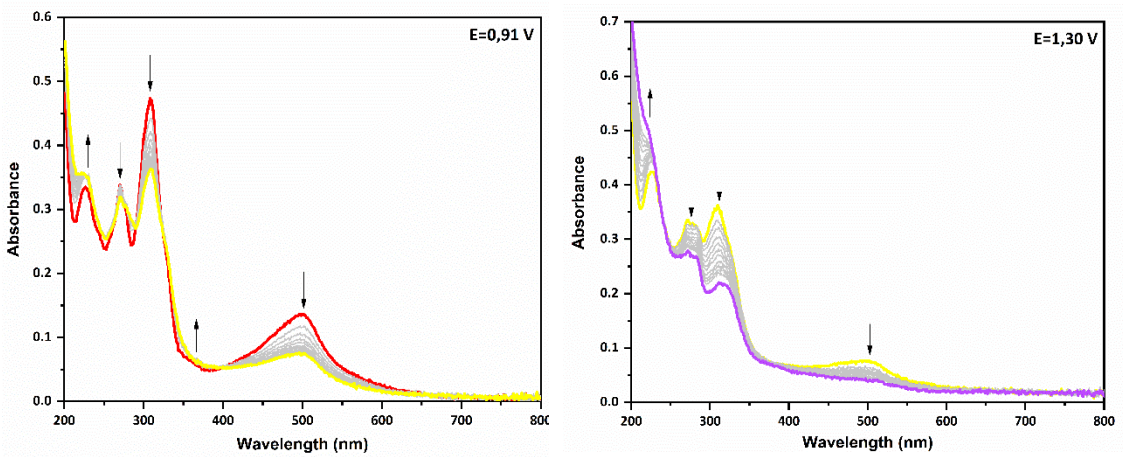

Figure 6 - Absorption spectra at different times (Δt=10 min) of complex (**3**) C = $2.3x10^{-4}$ M in $HClO_4$.

Spectrophotometric redox titration measurements gave results in agreement with those observed by spectroelectrochemistry. **Supplementary Figure S8** shows absorption spectra of complex **(3)** in 0.1 M $HClO_4$ after successive addition of aliquots of CAN until a total of 3 Ce(IV) equivalents were counted. When 2 Ce(IV) equivalents are added, absorbance of IL (λ_{max}=271 nm and 306 nm) and TCML (λ_{max}=494 nm) bands, due to metal centre oxidation from Ru^{II} to Ru^{IV}. Band at λ_{max}= 271 nm becomes more extended

and isosbestic points appear at λ=290, 322 and 410 nm. The resulting yellow spectrum corresponds to $[Ru^{IV}=O]^{2+}$ species. The addition of 1 more Ce (IV) equivalent results in complete bleaching of MLCT band due to the oxidation from Ru^{IV} to Ru^{V}. Intensity of IL band at λ_{max}=306 nm decreases and redshifts and isosbestic points appear at λ=266, 332 and 373 nm. The addition of 1 extra Ce (IV) equivalent does not produce any spectral change. The resulting purple spectrum is assigned to $[Ru^{V}=O]^{3+}$ species.

Supplementary Figures S9 and **S10** show results obtained by spectroelectrochemistry and spectrophotometric redox titration in 0.1 M $HClO_4$ for complex **(4)**.

WATER OXIDATION CATALYSIS

Aqua-complexes **(3)** and **(4)** catalyse water oxidation reaction by a water nucleophilic attack mechanism (WNA) to a metal-oxo species in agreement with that proposed for similar complexes. [60], [71]

Scheme 4 presents the catalytic cycle proposed for both complexes. **Table 4** summarises the potentials of the different redox couples, the rate constants of each step of the catalytic cycle and the catalytic activity parameters (overpotential η, turnover frequency TOF and turnover number TON) at pH=1.0, found for these complexes.

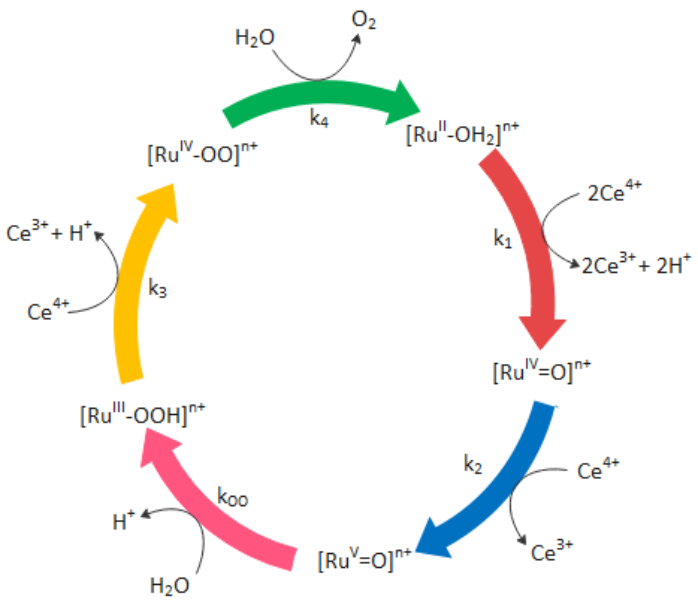

Scheme 4 - Proposed catalytic cycle for mononuclear complexes **(3)** and **(4)** in 0.1 M $HClO_4$ at T=25 °C.

Table 4 – Redox potentials, rate constants of catalytic cycle and catalytic activity parameters of some mononuclear ruthenium aqua complexes.

COMPLEX	$E_{1/2}$ (V) vs Ag/Ag (3M NaCl)			Rate constants					Catalytic activity parameters			Ref.
	III/II	IV/III	V/IV	k_1[a]	k_2[b]	k_3[c]	k_{OO}[d]	$k_{4\ cat.}$[e]	η [V]	TOF[f] (s^{-1})	TON	
(3)	0.91	≤0.91	1.25	0.25	0.0118	-	3.60	3.1	0.290	0.20	7.1	this work
(4)	1.02	≤1.02	1.27	0.39	0.0320	-	30.0	23	0.310	0.87	6.8	this work
$[Ru(tpy)(bpm)OH_2]^{2+}$	0.91	≤0.91	1.44	0.024	0.005	-	96	7.5	0.480	0.19	~7.5	[11], [59], [71]
$[Ru(tptz)(dmb)OH_2]^{2+}$	-	-	-	0.20	1.0	-	2.6	21	-	0.11	0.8	[24]
$[Ru(tptz)(bpy)OH_2]^{2+}$	0.95	≤0.95	1.30	0.94	0.280	-	1.5	17	0.340	0.23	2.6	[24]
$[Ru(tptz)(dcb)OH_2]^{2+}$	-	-	-	2.90	-	-	7.9	32	-	0.22	1.7	[24]
$[Ru(Me_2Ntpy)(bpy\text{-}OMe)(OH_2)]^{2+}$	0.51	0.94	1.16	-	-	-	-	-	0.200	1.5	6.7	[25]
$[Ru(tpy)(bpy)OH_2]^{2+}$	0.83	1.02	1.59	4.40	6.6	8.0	1.2	1.6	0.630	0.51	320	[11], [60], [67], [72]
$[Ru(tpy)(bpy\text{-}OMe)OH_2]^{2+}$	0.70	0.97	1.42	17	4.6	3.7	0.33	1.00*	0.460	1.10	100	[11], [60], [67], [72]
$[Ru(tpy)(dcb)OH_2]^{2+}$	0.95	-	1.68	rapid	330	-	1.00	4.3	0.720	0.20	460	[11], [60], [67], [72]

[a] $x10^4\ M^{-1}s^{-1}$. [b] $x10^3\ M^{-1}s^{-1}$. [c] $M^{-1}s^{-1}$. [d] $x10^{-4}\ s^{-1}$.[e] $x10^{-4}\ s^{-1}$.[f] $x10^{-3}\ s^{-1}$

* 1.1 $M^{-1}s^{-1}$

10.1002/ejic.202300021

Figure 7 shows kinetic profiles at λ_{max}=494 and 513 nm for complexes **(3)** and **(4)** respectively, after adding 4 equivalents of Ce(IV) to a solution of complex in 0.1 M $HClO_4$ at room temperature.

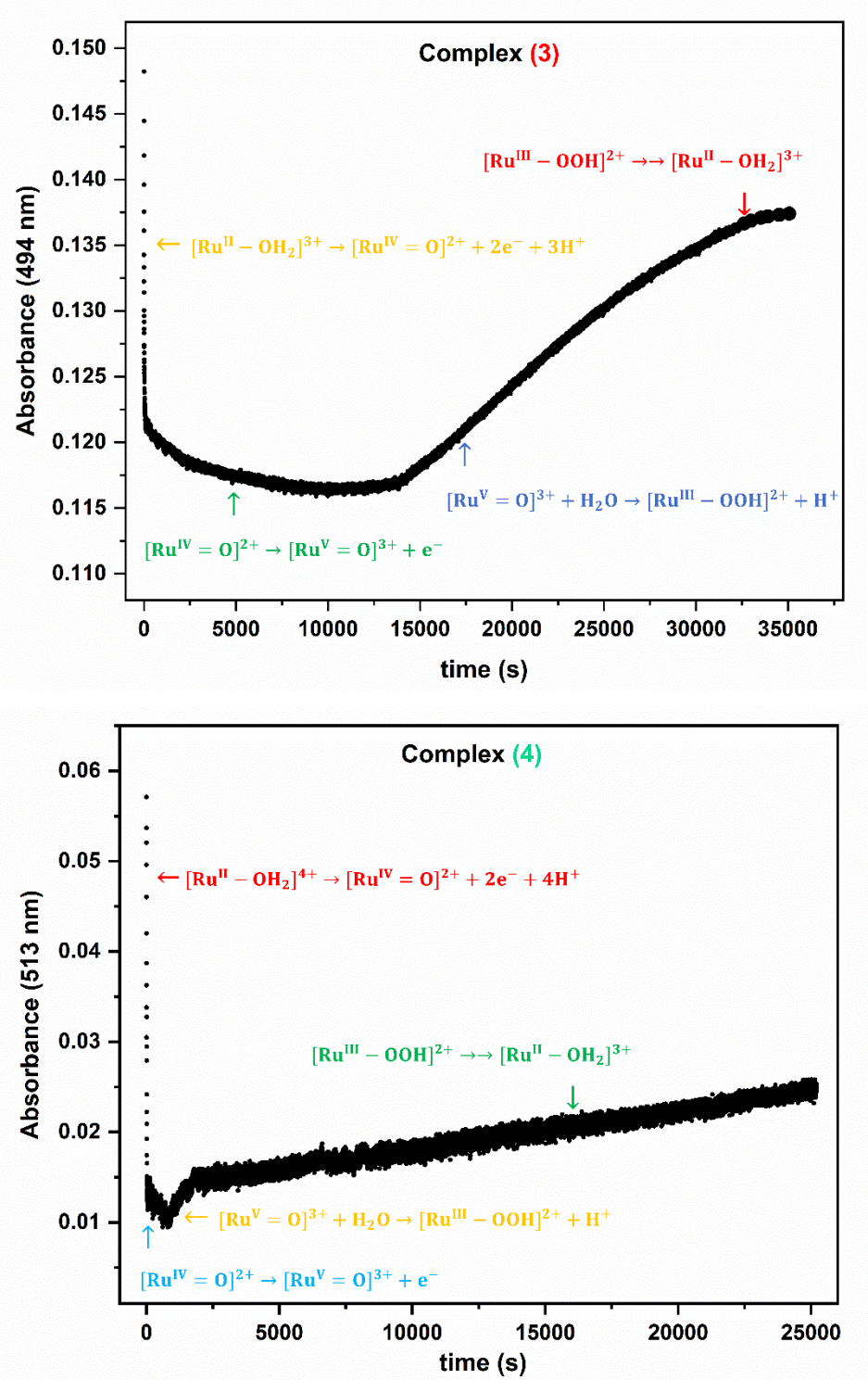

Figure 7 - Absorbance vs time for complexes **(3)** and **(4)** C=3.10^{-5} M in 0.1 M $HClO_4$ after adding 4 equivalents of Ce (IV) at T =25°C.

As seen in Supplementary **Figure S11** the first step involves metal centre oxidation from Ru^{II} to Ru^{IV}, **eq. 16**. k_1 was obtained by stopped-flow mixing of 2 equivalents of Ce(IV) with $[Ru^{II}\text{-}OH_2]^{n+}$ and recording absorbance-time changes at λ_{max}=494 nm and 513 nm for complexes **(3)** and **(4)** respectively, Supplementary **Figure S11 a**.

$$[Ru^{II} - OH_2]^{n+} + 2Ce^{4+} \xrightarrow{k_1} [Ru^{IV} = O]^{n+} + 2Ce^{3+} + nH^+ \quad \textbf{(16)}$$

The second step consists in oxidation from Ru^{IV} to Ru^{V}, **eq. 17**. This process was followed spectrophotometrically at λ_{max}=494 nm for complex **(3)** and λ_{max}=513 nm for **(4)** after addition 1 equivalent of Ce(IV) to $[Ru^{IV}=O]^{2+}$. k_2 value was obtained by fitting for a second order reaction (**Supplementary Figure S11 b)**.

$$[Ru^{IV} = O]^{2+} + Ce^{4+} \xrightarrow{k_2} [Ru^{V} = O]^{3+} + Ce^{3+} \quad \textbf{(17)}$$

Once formed, $[Ru^{V} = O]^{3+}$ species suffers nucleophilic attack by a water molecule of solvent, resulting in oxygen-oxygen bond formation and hydroperoxo intermediate $[Ru^{IV}\text{-}OO]^{2+}$ (eq 18). k_{OO} rate constant was determined from absorbance-time plot by using equation for a first order reaction, (**Supplementary Figure S11 c**).

$$[Ru^{V} = O]^{3+} + H_2O \xrightarrow{k_{OO}} [Ru^{III} - OOH]^{2+} + H^+ \quad \textbf{(18)}$$

Hydroperoxo intermediate produces peroxidic species $[Ru^{IV}\text{-}OO]^{2+}$ via a fast PCET reaction. k_3 could not be determined from stopped-flow kinetic measurements (**eq 19**). Under stoichiometric conditions $[Ru^{IV}\text{-}OO]^{2+}$ releases oxygen and regenerates catalyst complex, **eq 20**. $k_{st.}$ rate constant was determined by fitting with a first order velocity equation (**Supplementary Figure S11 d**).

$$[Ru^{III} - OOH]^{2+} + Ce^{4+} \xrightarrow{k_3} [Ru^{IV} - OO]^{2+} + Ce^{3+} + H^+ \quad \textbf{(19)}$$

$$[Ru^{IV} - OO]^{2+} + H_2O \xrightarrow{k_{4\,st.}} [Ru^{II} - OH_2]^{n+} + O_2 \quad \textbf{(20)}$$

Under catalytic conditions (30 eq. of Ce(IV)), dominant species of the catalytic cycle is $[Ru^{IV}\text{-}OO]^{2+}$. The kinetic of Ce(IV) consumptions is zero-order with respect to the oxidant, and the rate constant $k_{4cat.}$ was obtained by concentration-time plot, **Supplementary**

Figure S12. This reaction is rate-limiting step of catalytic cycle in agreement with that observed by Meyer for $[Ru(tpy)(bpm)OH_2]^{2+}$.[73]

To determine the TOF, solutions of complexes **(3)** and **(4)** (ca. $6.0x10^{-6}$ M - $6.5x10^{-5}$ M) and Ce(IV) in 0.1 M $HClO_4$ were prepared. 30 eq. of Ce(IV) was added to each solution and the reaction was monitored by using dissolved oxygen (DO) probe. TOF and order reaction with respect to catalyst were determined following the technique reported by Badiei et al.[74] Figure **8** shows OD vs time plot and logarithm of initial rate of oxygen evolution (v_{O2}) against logarithm of initial concentration of catalyst ($[cat]_0$) of complex **(4)**. **Supplementary Figure S13** shows results obtained for complex **(3)**.

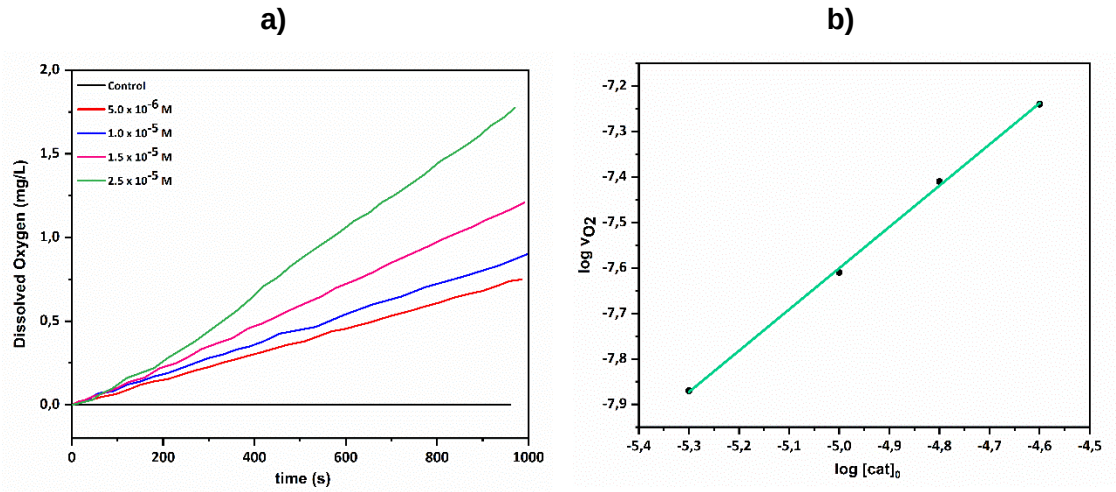

Figure 8 – a) Dissolved oxygen (mg/L) versus time for complex **(4)** in 0.1 M $HClO_4$ after addition of 30 equivalents of Ce (IV) at room temperature. **b)** log v_{O2} vs log $[cat]_0$.

For both complexes, the amount of oxygen evolved increases almost linearly with time and with catalyst concentration. Linear regression analysis showed that reaction follows first order kinetic with respect to the catalyst with a value of $\mathrm{TOF} = 2{,}0.10^{-4}\ \mathrm{s}^{-1}$ for complex **(3)** and $\mathrm{TOF} = 8{,}7.10^{-4}\ \mathrm{s}^{-1}$ for complex **(4)**.

To determine the TON of complex **(3)** and **(4)**, 30 equivalents of Ce (IV) were added to a solution of complex (final volume 6-8 mL) in 0.1 M $HClO_4$ and DO (mg/L) was recorded versus time until the reading remained constant. **Supplementary Figure S14** shows the OD vs time plots for complexes **(3)** and **(4)** with corresponding TON value found using **eq 21**.

$$\mathrm{TON} = \frac{\frac{\mathrm{OD(mg/L)}}{32\ \mathrm{mg/mmol}}\ .\ \text{total reaction volume}}{\text{mmol catalyst}} \qquad \textbf{(21)}$$

The TOF values calculated for complexes (4) is four time higher than that found for Dominguez et al for similar complexes [24] and four times higher than that for complex **(3),** while is in the same order of magnitude than those for the reported complex $[Ru(tpy)(bpy\text{-}OMe)(OH_2)]^{2+}$ and two time higher than that of $[Ru(tpy)(bpy)(OH_2)]^{2+}$. While the overpotential of complexes **(3)** and **(4)** are *ca* 2 times lower than that found for $[Ru(tpy)(bpm)(OH_2)]^{2+}$,[11,59,71] and $[Ru(tpy)(bpy)(OH_2)]^{2+}$[11,60,67,72] we have envisaged a good efficiency for the catalysts. The experimental TON value was 7.1 and 6.8 for complexes **(3)** and **(4)** respectively, very close to theoretical value of 7.5, indicating a high degree of recovery.

THEORICAL CALCULATIONS

Experimental data of complexes **(1)-(4)** were supported by theoretical DFT and TD-DFT calculations. **Supplementary Table T3** shows energy levels and contributions of each group to selected molecular orbital (MOs) of the synthesised complexes in methanol and **Figure 9** shows the energy diagrams and Kohn-Sham boundary MOs for complexes **(1)** and **(2)**.

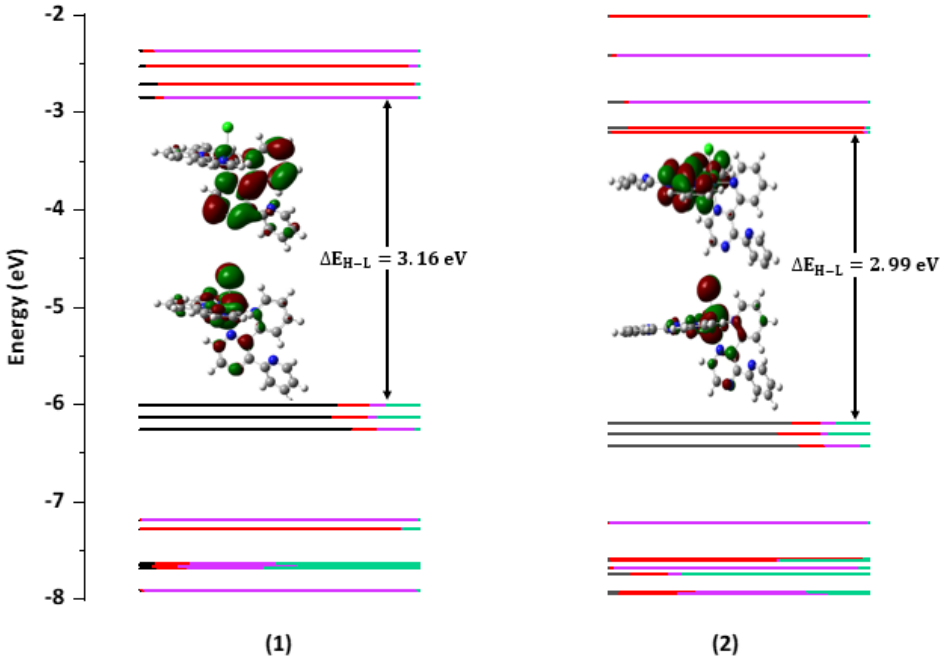

Figure 9 – Molecular Orbitals diagrams and Kohn-Sham boundary molecular orbitals calculated for complexes **(1)** and **(2)**. Contributions of the different groups to the OM: Ru (black), tpy and tptz (red), dpp (purple) and Cl^- (green).

HOMO orbitals of all complexes show a higher metallic character with slight contributions from ligands, while LUMO orbitals are predominantly located in aromatic ligands. If we compare complexes **(1)** and **(2)**, it is observed that HOMOs and LUMOs of complex **(2)** are stabilize 0.18 V and 0.35V respectively, due to the higher π-acceptor capacity of tptz with respect to tpy. Also, LUMOs of complex **(1)** is mainly centred on dpp ligand while for complex **(2)** it is centred on tptz ligand. By exchanging chloro for aqua ligand at the sixth position, a stabilisation of HOMO orbitals occurs due to lower donor character of water.

Figure 10 presents the MOs diagrams and Kohn-Sham boundary OMs of the different acid-base and redox species of complex **(3)** while **Supplementary Tables T4** and **T5** detail energies and percentage compositions of OMs from H-3 to L+3 of the acid-base species of complexes **(3)** and **(4)**. **Supplementary Figure S15** presents the Kohn-Sham boundary OMs for redox specie of complex **(4)** with their respective energies and percentage compositions.

10.1002/ejic.202300021

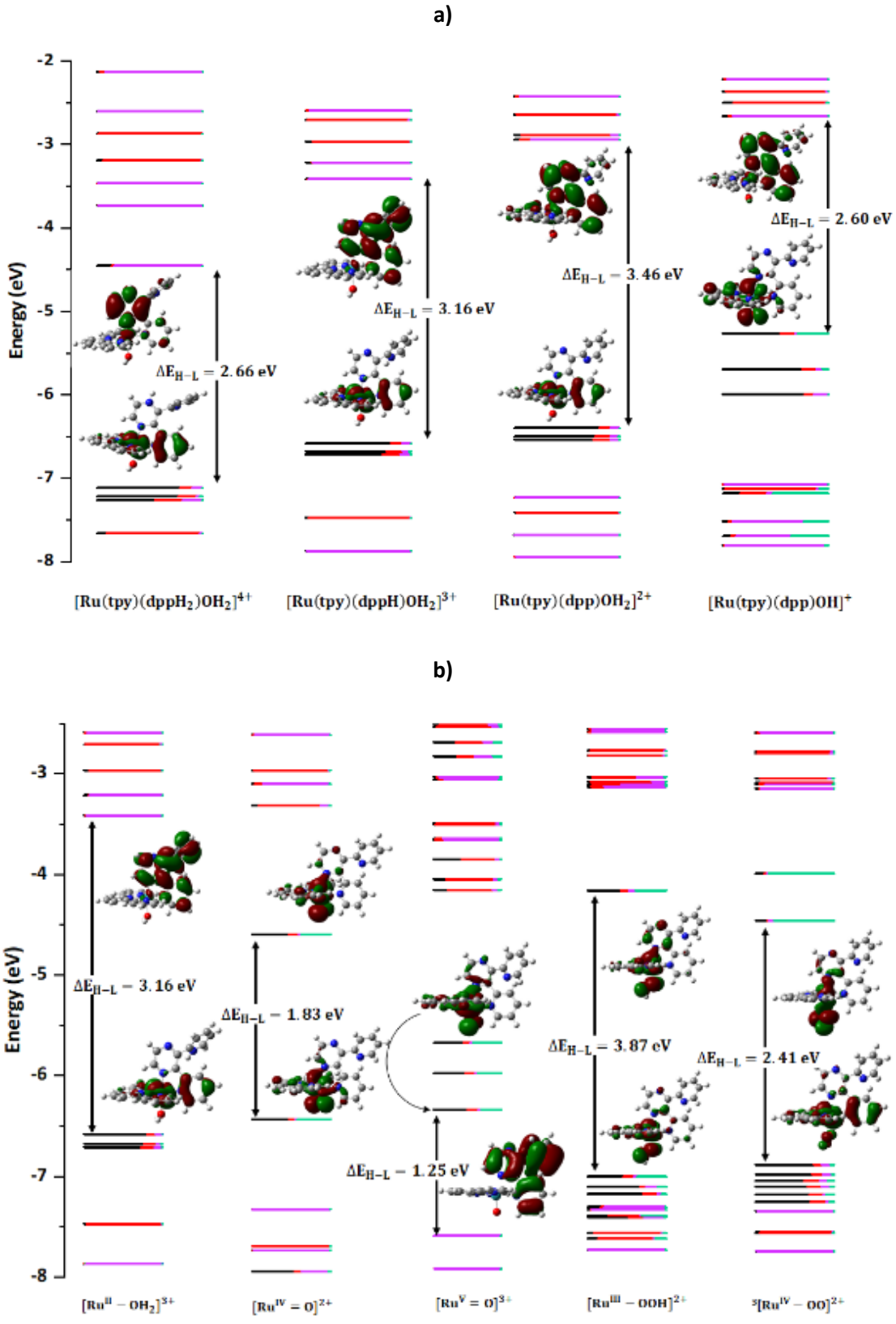

Figure 10 – MOs diagrams and Kohn-Sham boundary MOs calculated for complex (3). **a)** Acid-base species. **b)** Redox species. Contributions of the different groups to the OM: Ru (black), tpy (red), dpp (purple) and $OH_2/OH^-/O^{2-}/OOH^-/O_2^{2-}$ (green).

HOMOs of the acid-base species of both aqua-complexes are mainly centred on ruthenium atom while the LUMOs are aromatics. As polypyridine ligands deprotonate the boundary OMs are destabilised due to a decrease in π-acceptor character of these ligands, resulting in an increase in band gap energy. When aqua ligand is deprotonated, HOMO energy increases markedly as a result of the higher electron density donation of OH^- with respect to H_2O, decreasing the ΔE_{H-L}.

Redox species of complexes **(3)** and **(4)** at pH=1 show a strong decrease in band gap energy as metal centre is oxidised from Ru^{II} to Ru^{V} and increases the percentage contribution of ligands to HOMOs, while the opposite effect is observed in LUMOs. In $[Ru^{III}\text{-}OOH]^{2+}$ and $[Ru^{IV}\text{-}OO]^{2+}$ intermediates the ΔE_{H-L} increases, the HOMOs are predominantly metallic while in the LUMOs there is a strong contribution from the hydroperoxo and peroxo ligands, respectively.

$[Ru^{IV}\text{-}OO]^{2+}$ intermediate can exist in two spatial conformations, an open one in which the peroxo ligand binds to ruthenium via one oxygen atom (η^1), or a closed one when both oxygen atoms bind to it (η^2). Computational calculations of both spatial configurations, at singlet and triplet spin multiplicities, showed that the triplet species are more stable, as expected, since it is necessary that $[Ru^{IV}\text{-}OO]^{2+}$ intermediate has the same spin multiplicity as the released oxygen. On the other hand, we assume that there is an interconversion between two configurations due to the small energy difference between them, **Supplementary Figure S16**. Also, it was observed that metal-oxygen bond in triplet configuration is longer than in singlet configuration, which would favour oxygen release, while O-O bond is shorter and close to a double bond, **Supplementary Table T6**. These results agree with those reported by Meyer et al. for $[Ru(tpy)(bpm)OH_2]^{2+}$ [75] and by Dominguez for $[Ru(tptzH)(bpy)OH_2]^{3+}$.[58]

Figure 11 shows the calculated and experimental electronic spectra in methanol, and the electron density difference maps (EDDM) corresponding to the lowest energy transitions of chloro complexes **(1)** and **(2)** and aqua complexes **(3)** and **(4)**. **Supplementary Tables T7-T10** present the corresponding assignments. These theoretical results are in good agreement with the experimental spectroscopic and electrochemical data.

10.1002/ejic.202300021

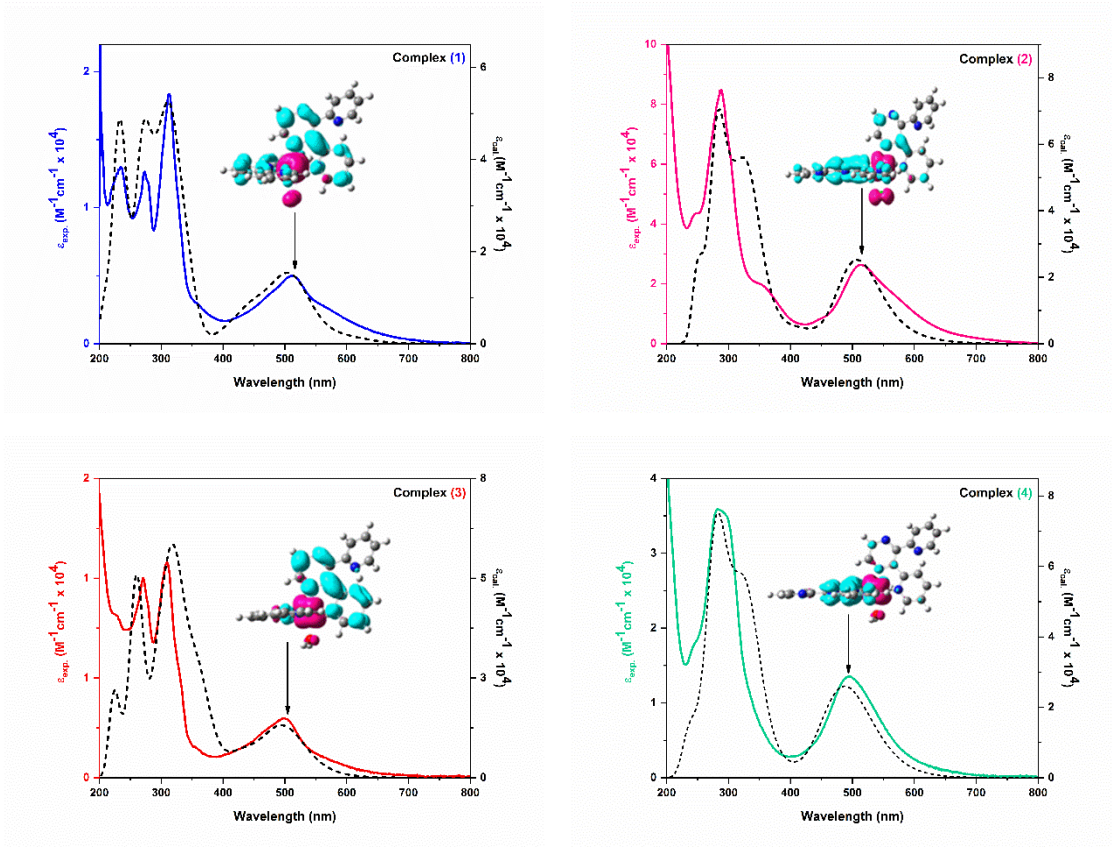

Figure 11 – Experimental (coloured solid line) and calculated (black dashed line) UV-visible spectra and EDDM for the lower energy transitions (in fuchsia areas of decreasing electron density and in turquoise areas of increasing electron density).

CONCLUSIONS

In this work we present the synthesis and physicochemical characterization of four new mononuclear ruthenium (II) complexes of molecular formula $[Ru(LLL)(dpp)X]^{n+}$ (with LLL=tpy= 2,2':6',2''-terpyridine; tptz=2,4,6-tris(2-pyridyl)-1,3,5-triazine, dpp=2,3-bis(2-pyridil)pyrazine and X=Cl^-, H_2O; n=1, 2). From the kinetic studies of complexes **(3)** and **(4)** at pH = 1, it was determined that the oxygen-oxygen bond formation takes place via WNA mechanism which consists of multiple PCET processes with the formation of low energy intermediates and that the rate-limiting step of the catalytic cycle is the release of dioxygen from the $[Ru^{IV}\text{-}OO]^{2+}$ intermediate. For both aqua-complexes a lower overpotential is observed compared to similar complexes list in **Table 4**. Complex **(4)** has a higher TOF than **(3)** and both complexes showed a yield above 90 %. These results indicate that both aqua-complexes are stable and active against water oxidation reaction. DFT and TD-DFT computational calculations showed good correlation with the experimental data.

EXPERIMENTAL SECTION

MATERIALS AND INSTRUMENTATION

All chemicals used in this work were analytical-reagent grade and used without further purification. $RuCl_3.3H_2O$, the ligands 2,2':6',2''-terpyridine (tpy), 2,3-bis(2-pyridyl)pyrazine (dpp) and 2,4,6-tris(2-pyridyl)-1,3,5-triazine (tptz) and salts of NH_4PF_6, $(NH_4)_2[Ce(NO_3)_6]$ and tetrakis-N-butylammonium hexafluorophosphate (TBAH), were purchased from Sigma-Aldrich Company. Elemental chemical analysis and X-ray diffraction were performed at INQUIMAE (University of Buenos Aires, Argentina). Mass spectra were obtained at CIBION-CONICET. Infrared spectra were recorded with a Perkin Elmer RX-1 FTIR spectrophotometer, using 1 cm quartz cells in KBr pellets. Cyclic voltammetry (CV) and Differential Pulse Voltammetry (DPV) experiments were carried out using a BAS EC Epsilon equipment, with vitreous C as a working electrode (WE), platinum wire as auxiliary electrode and Ag/AgCl (3M NaCl) as reference electrode (RE). Controlled potential electrolysis (CPE) and spectraelectrochemistry for complex (**3**) and **(4)** were performed in 0.1 M CF_3COOH using a HoneyComb Cell Spectro de Pine Research with a mesh Au working electrode, Au bands as counter electrode and Ag/AgCl (3 M NaCl) as the reference electrode. Kinetic experiments were performed on Applied Photophysics equipment connected to a bath thermostated to 0.5 °C, attached to the UV-vis spectrophotometer. Data collection was done using Kinetics and Scanning Kinetics CaryWinUV software package.

Catalytic activity measurements were performed with a Hanna Instruments HI 9146N dissolved oxygen sensor.

COMPUTATIONAL PROCEDURES

DFT calculations were carried out with Gaussian-03 program package.[76] All molecules were optimized using Becke's three-parameter hybrid functional B3LYP.[77] LANL2DZ basis[78] set was used for all atoms. No symmetry restrictions were placed on the geometry optimizations and, depending on the spin multiplicity, restricted or unrestricted Kohn–Sham approximations were considered. Tight convergence criteria were used for geometry optimizations and ultrafine grid in all calculations. To include solvent polarization effects, the calculations were done by using the conductor-like polarizable continuum model (CPCM).[79] The contribution of different groups on the orbitals, electron density difference maps (EDDM), calculated UV-vis spectra and transitions related to them were obtained using the GaussSum Version 3.0 Program.[80] UV-vis

profiles were obtained by considering a typical half-bandwidth of $\Delta\nu_{1/2}$ =3000 cm^{-1} for all electronic transitions. TD-DFT calculations were done by considering 100 states to simulate all UV-vis spectra.

SYNTHESES

[Ru(tpy)(dpp)Cl]PF$_6$.3.5H$_2$O (1). 200 mg (0.454 mmol) of $[\mathrm{Ru(tpy)Cl_3}]$ and 111.5 mg (0.476 mmol) of dpp ligand were dissolved in 3 mL of ethylene glycol. Solution was heated at reflux during 2 hours with vigorous stirring in an oil bath. Orange solution was cooled to room temperature and 4 mL of absolute ethanol was added. It was filtered to remove unreacted $[\mathrm{Ru(tpy)Cl_3}]$. Then 40 mL of diethyl ether was added and cooling in a freezer overnight. Solid precipitated was filtered and washed with 8 mL of diethyl ether:ethanol (2:1) and 24 mL diethyl ether. It was dried under vacuum over $\mathrm{P_4O_{10}}$.
Recrystallisation: the solid was dissolved in a small volume of ethanol and filtered. Precipitated with diethyl ether and stored in freezer. The solid was filtered and dried under vacuum over $\mathrm{P_4O_{10}}$
Yield: 206.7 mg (65.0%). *Chemical Analysis.* Calculated values for $\mathrm{RuC_{29}H_{28}N_7O_{3,5}Cl_2}$ (702.5 g/mol): % C 49.6, % H 4.0, % N 14.0. Experimental values: % C 49.5, % H 4.1, % N 14.0.
Finally, 206.7 mg of $\mathrm{[Ru(tpy)(dpp)Cl]Cl.3{,}5H_2O}$ was dissolved in a small volume of water and 415 mg of $\mathrm{NH_4PF_6}$ in 1 mL of water was added. It was cooled in freezer, filtered and washed with a small volume of cold water. Dried under vacuum over $\mathrm{P_4O_{10}}$. *Yield:* 230 mg (96%) of $\mathrm{[Ru(tpy)(dpp)Cl]PF_6.3.5H_2O}$. ESI-MS (MeOH): m/z=604.1 ([M]$^+$), **Supplementary Figure S17 a**

$\mathrm{[Ru(tptz)(dpp)Cl]PF_6.4H_2O}$ (2). 245 mg (0.471 mmol) of $[\mathrm{Ru(tptz)Cl_3}]$ and 116 mg (0.494mmol) of dpp ligand were dissolved in 3 mL of ethylene glycol. The solution was heated at reflux during 2 hours with vigorous stirring in an oil bath. Brown solution was cooled to room temperature and 4 mL of absolute ethanol was added. It was filtered to remove unreacted $[\mathrm{Ru(tptz)Cl_3}]$. 40 mL diethyl ether was added and cooled in a freezer overnight. The solid was filtered and washed with 8 mL of diethyl ether:ethanol (2:1) and finally with 24 mL of diethyl ether. It was dried under vacuum over $\mathrm{P_4O_{10}}$. The solid was dissolved in water, 480 mg $\mathrm{NH_4PF_6}$ in 1 mL of water was added and cooled in refrigerator, filtered and washed with a small volume of cold water. It was dried under vacuum over $\mathrm{P_4O_{10}}$. The brown solid obtained was purified by column chromatography (stationary

phase: activated alumina, mobile phase: toluene:methanol:acetone (4:1:1 v/v)). The first eluted fraction, containing the desired product, was collected and concentrated by a rotary evaporator and the solid was precipitated with ethyl ether, filtered and dried under vacuum over P_4O_{10}.

Yield: 105.9 mg (25%). Chemical analysis. Calculated values for $RuC_{32}H_{30}N_{10}O_4ClPF_6$ (900.1g/mol): %C 42.7, %H 3.4, %N 15.6. Experimental values: %C 43.7, %H 3.5, %N 14.6. ESI-MS (MeOH):m/z=828.0([M]PF_6), m/z= 683.1 ([M]$^+$), **Supplementary Figure S17 b.**

$\mathbf{[Ru(tpy)(dpp)(OH_2)](PF_6)_2 . 3.5H_2O}$ **(3)**. 39.0 mg (0.048 mmol) of complex **(1)** and 13.4 mg (0.053mmol) of $AgPF_6$ were dissolved in 10 mL of an acetone: water (1.5:1 v/v) mixture and heated at reflux in dark and under argon stream for 2 hours with vigorous stirring. The reddish solution was cooled at room temperature, centrifuged for 5 to 10 minutes and filtered through filter paper to remove $AgCl$. The acetone was evaporated and 100 mg NH_4PF_6 in 0.5 mL of water was added and cooled in refrigerator. The solid was filtered and washed with small portions of cold water. It was dried under vacuum over P_4O_{10}. *Yield:* 38.3 mg (85%). *Chemical analysis*. Calculated values for $RuC_{29}H_{30}N_7O_{3,5}P_2F_{12}$ (939.5 g/mol): %C 37.1, %H 3.2, %N 10.5. Experimental values: %C 36.2, %H 2.9, %N 10.5. ESI-MS (MeOH): $m/z = 284.5$ ([M-H_2O]$^{2+}$), **Supplementary Figure S17 c.**

$\mathbf{[Ru(tptz)(dpp)(OH_2)](PF_6)_2 . 4H_2O}$ **(4).** 22.0 mg (0.024mmol) of complex **(2)** and 6.6 mg (0.026 mmol) of $AgPF_6$ were dissolved in 7.5 mL of an acetone: water mixture (1.5:1 v/v) mixture. Solution was heated at reflux in dark and under argon stream for 2 hours with vigorous. The reddish solution was cooled at room temperature, centrifuged for 5 to 10 minutes and filtered through filter paper to remove $AgCl$. The acetone was evaporated and 50 mg NH_4PF_6 in 0.5 mL of water was added and cooled in the refrigerator. The solid was filtered and washed with small portions of cold water. It was dried under vacuum over P_4O_{10}. *Yield*: 18.3 mg (74.1%). *Chemistry analysis*: calculated values for $RuC_{32}H_{32}N_{10}O_5P_2F_{12}$ (1027.7 g/mol): %C 37.4, %H 3.1, %N 13.6. Experimental values: %C 36.8, %H 2.9, %N 13.1. ESI-MS (MeOH): $m/z = 333.0$ ([M]$^{2+}$), **Supplementary Figure S17 d**

Appendix A. Supplementary data

CCDC 2235216 contains the supplementary crystallographic data for complex (4). Summary Data -Deposition Number 2235216. Compound Name: $[\mathbf{Ru(tptz)(dpp)(OH_2)}](\mathbf{PF_6})_2 . \mathbf{4H_2O}$. Data Block Name: data_shelx.

Unit Cell Parameters: a 23.7407(10) b 12.4009(5) c 25.4660(12) C2/c. These data can be obtained free of charge via http://www.ccdc.cam.ac.uk/conts/retrieving.html, or from the Cambridge Crystallographic Data Centre, 12 Union Road, Cambridge CB2 1EZ, UK; fax:

(+44) 1223-336-033; or e-mail: deposit@ccdc.cam.ac.uk. Supplementary data associated with this article can be found, in the online version.

AUTHOR CONTRIBUTIONS

Prof. Dra. A. M. Peyrot, synthesis, characterization investigation, kinetics measurements and writing. Prof. Lic. M.P. Zelaya kinetics measurements and writing. Prof. Dr. P Alborés X-ray diffraction. Prof. Dra. F. Fagalde supervision, writing, review and editing.

CONFLICTS OF INTEREST

There are no conflicts to declare.

ACKNOWLEDGEMENTS

We thank Consejo Nacional de Investigaciones Científicas y Técnicas (CONICET), Agencia Nacional de Promoción Científica y Tecnológica (ANPCyT) and Universidad Nacional de Tucumán (UNT), all from Argentina, for financial support. A. M. P. and M.P. Zelaya thanks CONICET for graduate fellowships. F. F. and P. A. are Members of the Research Career (CONICET).

KEY WORDS

Aquo mononuclear Ru(II) complexes; DFT and TD-DFT calculations; 2,3-bis(2-pyridyl)pyrazine; ruthenium(II) complexes; water oxidation**.**

NOTES AND REFERENCES

[1] N. Armaroli, V. Balzani, *Angew. Chemie Int. Ed.*, **2007**, *46*, 52–66,

[2] T. Bak, J. Nowotny, M. Rekas, C. C. Sorrell, *Int. J. Hydrogen Energy*, **2002**, *27*, 991–1022,.

[3] R. M. Navarro Yerga, M. C. Álvarez Galván, F. Del Valle, J. A. Villoria de la

Mano, J. L. G. Fierro, *ChemSusChem Chem. Sustain. Energy Mater.*, **2009**, 2, 471–485,.

[4] R. M. Navarro, F. Del Valle, J. A. V. De La Mano, M. C. Álvarez-Galván, J. L. G. Fierro, *Adv. Chem. Eng.*, **2009**, *36*, 111–143,.

[5] M. Tahir , *Nano Energy*, **2017**, *37*, 136–157,.

[6] X. Sala, I. Romero, M. Rodríguez, L. Escriche, A. Llobet, *Angew. Chemie Int. Ed.*, **2009**, *48*, 2842–2852,.

[7] S. Romain, L. Vigara, A. Llobet, *Acc. Chem. Res.*, **2009**, *42*, 1944–1953,.

[8] J. J. Concepcion , *Acc. Chem. Res.*, **2009**, *42*, 1954–1965.

[9] C. Herrero, B. Lassalle-Kaiser, W. Leibl, A. W. Rutherford, A. Aukauloo, *Coord. Chem. Rev.*, **2008**, *252,* 456–468.

[10] D. Gust, T. A. Moore, A. L. Moore, *Acc. Chem. Res.*, **2009**, *42*, 1890–1898.

[11] M. D. Karkas, O. Verho, E. V Johnston, B. Åkermark, *Chem. Rev.*, **2014,** *114*, 11863–12001.

[12] C.-F. Leung , *Energy Environ. Sci.*, **2012**, *5*, 7903–7907.

[13] S. Berardi, *J. Am. Chem. Soc.*, **2012**, *134*, 11104–11107.

[14] J. L. Fillol, Z. Codolà, I. Garcia-Bosch, L. Gómez, J. J. Pla, M. Costas, *Nat. Chem.*, **2011**, *3*, pp. 807–813.

[15] L. Xiao, Z. Wang, J. Guan, *Coord. Chem. Rev.*, **2022**, *472*, 214777.

[16] X. Bai, Z. Duan, B. Nan, L. Wang, T. Tang, J. Guan, *Chinese J. Catal.*, **2022**, *43*, 2240–2248.

[17] X. Bai, L. Wang, B. Nan, T. Tang, X. Niu, J. Guan, *Nano Res.*, **2022**, *15*, 6019–6025.

[18] T. Tang, S. Li, J. Sun, Z. Wang, J. Guan, *Nano Res.*, **2022**, *15*, 8714–8750.

[19] Q. Zhang and J. Guan, *Nano Res.*, **2022**, *15*, 38–70.

[20] M. Yagi and M. Kaneko, *Chem. Rev.*, **2001**, *101*, 21–36.

[21] Y. Qu and X. Duan, *Chem. Soc. Rev.*, **2013**, *42*, 2568–2580.

[22] B. M. Hunter, H. B. Gray, A. M. Muller, *Chem. Rev.*, **2016**, *116*, 14120–14136.

[23] S. Ye, C. Ding, M. Liu, A. Wang, Q. Huang, C. Li, *Adv. Mater.*, **2019**, *31* , 1902069.

[24] S. E. Domínguez, F. E. M. Vieyra, F. Fagalde, *Dalt. Trans.*, **2020**, *49*, 12742 – 12755.

[25] P. O. Abate, A. M. Peyrot, X. Fontrodona, I. Romero, F. Fagalde, N. E. Katz, *RSC Adv.*, **2022**, *12*, 8414–8422.

[26] B. Zhang, L. Sun, *Chem. Soc. Rev.*, **2019**, *48*, 2216–2264.

[27] L. Tong, R. P. Thummel, *Chem. Sci.*, **2016**, *7*, 6591–6603.

[28] Y. Pushkar, D. Moonshiram, V. Purohit, L. Yan, I. Alperovich, *J. Am. Chem.*

Soc., **2014**, *136*, 11938–11945.

[29] A. K. Ravari *, J. Am. Chem. Soc.*, **2019**, *142*, 884–893.

[30] Y. Pineda-Galvan *J. Catal.*, **2019**, *375,* 1–7.

[31] A. Kimoto, K. Yamauchi, M. Yoshida, S. Masaoka, K. Sakai, *Chem. Commun.*, **2012**, *48*, 239–241.

[32] J. J. Concepcion , *Proc. Natl. Acad. Sci.*, **2012**, *109*, 15669–15672.

[33] T. Kikuchi, K. Tanaka, *Eur. J. Inorg. Chem.*, **2014**, 607–618.

[34] X. Sala, S. Maji, R. Bofill, J. García-Antón, L. Escriche, A. Llobet, *Acc. Chem. Res.*,**2014**, *47*, 504–516.

[35] Z. Chen, J. J. Concepcion, X. Hu, W. Yang, P. G. Hoertz, T. J. Meyer, *Proc. Natl. Acad. Sci.*, **2010**, *107*, 7225–7229.

[36] X. Zhang , *J. Am. Chem. Soc.*,**2022**, *144,* 17748–17752.

[37] H.-Y. Du, S.-C. Chen, X.-J. Su, L. Jiao, M.-T. Zhang, *J. Am. Chem. Soc.*, **2018**, *140*, 1557–1565.

[38] H. Zhang, X. Su, F. Xie, R. Liao, M. Zhang, *Angew. Chemie*, 2021, 133, 12575–12582.

[39] B. Limburg, E. Bouwman, S. Bonnet, *Coord. Chem. Rev.*, **2012**, *256*, 1451–1467.

[40] Y. M. Badiei, *Inorg. Chem.*, 2013, 52, 8845–8850.

[41] B. P. Sullivan, J. M. Calvert, T. J. Meyer, *Inorg. Chem.*, **1980**, *19,* 1404–1407.

[42] D. C. Ware, P. A. Lay, H. Taube, M. H. Chou, C. Creutz, *Inorg. Synth.*, **1986**, 299–306.

[43] K. J. Takeuchi, M. S. Thompson, D. W. Pipes, T. J. Meyer, *Inorg. Chem.***1984**, *23*, 1845–1851.

[44] H.-W. Tseng, R. Zong, J. T. Muckerman, R. Thummel, *Inorg. Chem.*, **2008**, *47*, 11763–11773.

[45] C. M. Hartshorn, K. A. Maxwell, P. S. White, J. M. DeSimone, T. J. Meyer, *Inorg. Chem.*, **2001**, *40,* 601–606.

[46] C. Sens, M. Rodríguez, I. Romero, A. Llobet, T. Parella, J. Benet-Buchholz, *Inorg. Chem.*, **2003**, *42*, 8385–8394.

[47] X.-L. Hong, H. Chao, C.-S. Xi, X.-L. Wang, L.-N. Ji, *Anal. Sci. X-ray Struct. Anal. Online*, **2004**, *20*, x49–x50..

[48] M. Daryanavard, H. Hadadzadeh, A. D. Khalaji, M. Weil, *Transit. Met. Chem.*, **2009**, *34*, 779–786.

[49] V. S. Mane, A. S. Kumbhar, R. P. Thummel, *Dalt. Trans.*, **2017**, *46*, 12901–12907.

[50] M. M. Milutinović , *Dalt. Trans.*, **2017**, *46*, 2360–2369.

[51] A. M. Heyns, *Spectrochim. Acta Part A Mol. Spectrosc.*,**1977**, *33*, 315–322.

[52] L. M. Vogler, K. J. Brewer, *Inorg. Chem.*, **1996**, *35*, 818–824..

[53] J.-D. Lee, L. M. Vrana, E. R. Bullock, K. J. Brewer, *Inorg. Chem.*, 1998, *37*, 3575–3580.

[54] S. Swavey, Z. Fang, K. J. Brewer, *Inorg. Chem.*, **2002**, *41,* 2598–2607.

[55] S. Bonnet, J.-P. Collin, N. Gruber, J.-P. Sauvage, E. R. Schofield, *Dalt. Trans.*, **2003**, *24*, 4654–4662.

[56] S. Ghumaan, S. Kar, S. M. Mobin, B. Harish, V. G. Puranik, G. K. Lahiri, *Inorg. Chem.*, **2006,** *45,* 2413–2423.

[57] E. Jakubikova, *Inorg. Chem.*, **2009**, *48*, 10720–10725.

[58] S. E. Domínguez, F. E. Moran-Vieyra, F. Fagalde, *Dalt. Trans.*,**2020**, *49,* 12742–12755.

[59] J. J. Concepcion, J. W. Jurss, J. L. Templeton, T. J. Meyer, *J. Am. Chem. Soc.*, **2008**, *130*, 16462–16463.

[60] D. J. Wasylenko, C. Ganesamoorthy, M. A. Henderson, B. D. Koivisto, H. D. Osthoff, C. P. Berlinguette, *J. Am. Chem. Soc.*, **2010**, *132*, 16094–16106.

[61] K. J. Brewer, W. R. Murphy Jr, S. R. Spurlin, J. D. Petersen,*Inorg. Chem.*,**1986,** *25*, 882–884.

[62] N. E. Tokel-Takvoryan, R. E. Hemingway, A. J. Bard, *J. Am. Chem. Soc.*, **1973**, *95*, 6582–6589.

[63] T. Saji, S. Aoyagui, *J. Electroanal. Chem. Interfacial Electrochem.,***1980***, 110*, 329–334.

[64] N. Kaveevivitchai, R. Chitta, R. Zong, M. El Ojaimi, R. P. Thummel, *J. Am. Chem. Soc.*, **2012**, *134*,10721–10724.

[65] S. Campagna, G. Denti, G. De Rosa, L. Sabatino, M. Ciano, V. Balzani, *Inorg. Chem.*, **1989**, *28*, 2565–2570.

[66] D. R. Weinberg , *Chem. Rev.*,**2012**, *112,* 4016–4093.

[67] D. J. Wasylenko, C. Ganesamoorthy, M. A. Henderson, C. P. Berlinguette, *Inorg. Chem.*, **2011**, *50,* 3662–3672.

[68] D. E. Polyansky, J. T. Muckerman, J. Rochford, R. Zong, R. P. Thummel, E. Fujita, *J. Am. Chem. Soc.*, **2011**, *133*, 14649–14665.

[69] T. J. Meyer, M. H. V. Huynh, *Inorg. Chem.*, **2003**, *42*, 8140–8160.

[70] M. H. V Huynh, T. J. Meyer, *Chem. Rev.*, **2007**, *107,* 5004–5064.

[71] J. J. Concepcion, M.-K. Tsai, J. T. Muckerman, T. J. Meyer*, J. Am. Chem. Soc.,**2010**,* 132, 1545–1557.

[72] D. J. Wasylenko, C. Ganesamoorthy, B. D. Koivisto, M. A. Henderson, C. P. Berlinguette, *Inorg. Chem.*,**2010**, *49*, 2202–2209.

[73] Y. M. Badiei , *Inorg. Chem.*, **2013**, *52*, 8845–8850.

[74] G. Renderos, T. Aquino, K. Gutierrez, Y. M. Badiei, *J. Chem. Educ.*, **2017**, *94*, 922–927.

[75] X. Lin , *Proc. Natl. Acad. Sci.*, **2012**, *109*, 15669–15672.

[76] Mj. Frisch "Gaussian 03, revision D. 02," **2004**.

[77] R. H. Hertwig, W. Koch, *Chem. Phys. Lett.*, **1997**, *268*, 345–351.

[78] S. Chiodo, N. Russo, E. Sicilia, *J. Chem. Phys.*, **2006**, *125*, 104107.

[79] M. Cossi, N. Rega, G. Scalmani, V. Barone, *J. Comput. Chem.*, **2003**, *24*, 669–681.

[80] N. M. O'boyle, A. L. Tenderholt, K. M. Langner, *J. Comput. Chem.*, **2008,** *29*, 839–845.

10.1002/ejic.202300021

TABLE OF CONTENTS

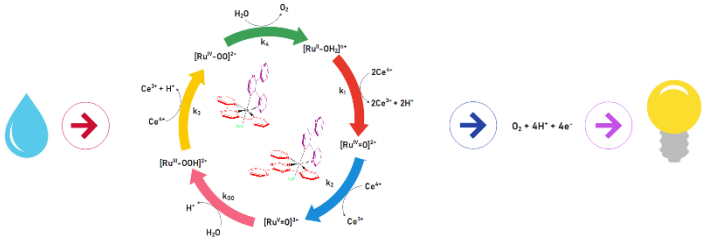

Synthesis and characterization of new chloro and aqua mononuclear Ru(II) complexes of formula $[Ru(tpy/tptz)(dpp)Cl]PF_6$ and $[Ru(tpy/tptz)(dpp)H_2O](PF_6)_2$ with tpy=2,2′:6’,2”-terpyridine; tptz=2,4,6-tris(2-pyridyl)-1,3,5-triazine and dpp=2,3-bis(2-pyridil)pyrazine useful for water oxidation catalysts at pH = 1 using Ce(IV)